The Astrophysical Journal, 726:39 (21pp), 2011 January 1 doi:10.1088/0004-637X/726/1/39

A SURVEY OF DIFFUSE INTERSTELLAR BANDS IN THE ANDROMEDA GALAXY: OPTICAL SPECTROSCOPY OF M31 OB STARS

Martin A. Cordiner[1,7,8], Nick L. J. Cox[2,9], Christopher J. Evans[3], Carrie Trundle[4], Keith T. Smith[5], Peter J. Sarre[5], and Karl D. Gordon[6]

[1] Astrochemistry Laboratory and The Goddard Center for Astrobiology, Mailstop 691, NASA Goddard Space Flight Center, 8800 Greenbelt Road, Greenbelt, MD 20770, USA; martin.cordiner@nasa.gov
[2] Institute for Astronomy, K.U. Leuven, Celestijnenlaan 200D, Bus 2401, Leuven, Belgium
[3] UK ATC, Royal Observatory Edinburgh, Blackford Hill, Edinburgh EH9 3HJ, UK
[4] Astrophysics Research Centre, School of Mathematics and Physics, Queen's University, Belfast BT7 1NN, UK
[5] School of Chemistry, The University of Nottingham, University Park, Nottingham NG7 2RD, UK
[6] Space Telescope Science Institute, Baltimore, MD 21218, USA
Received 2010 March 9; accepted 2010 October 30; published 2010 December 13

ABSTRACT

We present the largest sample to date of intermediate-resolution blue-to-red optical spectra of B-type supergiants in M31 and undertake the first survey of diffuse interstellar bands (DIBs) in this galaxy. Spectral classifications, radial velocities, and interstellar reddenings are presented for 34 stars in three regions of M31. Based on a subset of these stars with foreground-corrected reddening $E_{B-V}^{\mathrm{M31}} \geqslant 0.05$, the strengths of the M31 DIBs are analyzed with respect to the amount of dust, ultraviolet radiation field strength, and polycyclic aromatic hydrocarbon emission flux. Radial velocities and equivalent widths are given for the λ5780 and λ6283 DIBs toward 11 stars. Equivalent widths are also presented for the following DIBs detected in three sightlines in M31: λλ4428, 5705, 5780, 5797, 6203, 6269, 6283, 6379, 6613, 6660, and 6993. All of these M31 DIB carriers reside in clouds at radial velocities matching those of interstellar Na I and/or H I. The relationships between DIB equivalent widths and reddening (E_{B-V}^{M31}) are consistent with those observed in the local interstellar medium (ISM) of the Milky Way (MW). Many of the observed sightlines show DIB strengths (per unit reddening) which lie at the upper end of the range of Galactic values. DIB strengths per unit reddening are found (with 68% confidence) to correlate with the interstellar UV radiation field strength. The strongest DIBs are observed where the interstellar UV flux is lowest. The mean *Spitzer* 8/24 μm emission ratio in our three fields is slightly lower than that measured in the MW, but we identify no correlation between this ratio and the DIB strengths in M31. Interstellar oxygen abundances derived from the spectra of three M31 H II regions in one of the fields indicate that the average metallicity of the ISM in that region is $12 + \log[\mathrm{O/H}] = 8.54 \pm 0.18$, which is approximately equal to the value in the solar neighborhood.

Key words: dust, extinction – galaxies: individual (M31) – galaxies: ISM – H II regions – ISM: lines and bands – stars: early-type

Online-only material: color figures

1. INTRODUCTION

Over 400 diffuse interstellar bands (DIBs) are now known (Hobbs et al. 2008, 2009), but the identity of the carriers has remained a mystery since their discovery almost 90 years ago. DIBs arise predominantly in the diffuse atomic component of the interstellar medium (ISM; Snow & McCall 2006), and it is debated whether they are attributable to interstellar gas or dust (see the review by Sarre 2006). Substructure observed in several DIB profiles indicates that the carriers of these DIBs are probably large, stable, UV-resistant gas-phase molecules (Sarre et al. 1995; Ehrenfreund & Foing 1996). Likely carrier candidates include organic molecules such as polycyclic aromatic hydrocarbons (PAHs), fullerenes, and carbon chains (see, e.g., Salama et al. 1996; Ruiterkamp et al. 2005).

The study of DIB strengths in extragalactic environments allows analysis of the carrier formation and destruction mechanisms under physical and chemical conditions that may be quite distinct from those typically found in the Milky Way (MW). Galaxies in the Local Group thus provide us with alternative astrochemical laboratories and opportunities for detailed studies of interstellar chemistry over a broad range of conditions that may be uncommon or nonexistent in the ISM of our Galaxy. Previous extragalactic DIB research has been reviewed by Snow (2002b). Recent research in this area has made significant progress using 10 m class telescopes. Atoms, molecules, and DIBs have been studied in the Small and Large Magellanic Clouds (MCs) using optical absorption spectroscopy (e.g., Ehrenfreund et al. 2002; Cox et al. 2006, 2007; Cordiner 2006; Welty et al. 2006). The effects on DIB carrier abundances of the different physical and chemical interstellar conditions were examined, including the higher gas-to-dust ratios, lower metallicities, different-shaped extinction curves, and stronger interstellar radiation fields (ISRFs)—identifying in particular the dependence of DIB strengths (per unit reddening) on the interstellar metallicity. Beyond the Local Group, there have been relatively few studies, which have generally been confined to sightlines probed by bright supernovae (Rich 1987; D'Odorico et al. 1989; Steidel et al. 1990; Sollerman et al. 2005; Cox & Patat 2008; Thoene et al. 2009) or background quasars (e.g., York et al. 2006; Ellison et al. 2008; Lawton et al. 2008).

Desirable attributes of galaxies for detailed optical spectroscopic absorption studies of the ISM include proximity, an

[7] Formerly at Astrophysics Research Centre, School of Mathematics and Physics, Queen's University, Belfast BT7 1NN, UK.
[8] Working under cooperative agreement with Department of Physics, The Catholic University of America, Washington, DC 20064, USA.
[9] Formerly at Herschel Science Centre, European Space Astronomy Centre, ESA, P.O. Box 78, E-28691 Villanueva de la Cañada, Madrid, Spain.

abundance of OB-type supergiants, Doppler velocities greater than $\sim$100 km s^{-1} (to distinguish extragalactic spectroscopic features from those arising in the MW foreground), and a relatively low foreground extinction. Beyond the MCs, the obvious candidates for study are the spiral galaxies M31 and M33. However, these galaxies are more than 10 times more distant than the MCs, so high-resolution spectra are not readily obtained using current telescopes; surveys of large numbers of stars are only feasible at low-to-intermediate spectral resolution. The matter in M31 spans a range of radial velocities between around 0 and 600 km s^{-1} (see Figure 4), so the majority of spectral features are easily separable from those in the MW, even at modest resolving power. However, as we identify in this study, toward the northern edge of M31 the Doppler separation of spectral features can be sufficiently small to cause difficulty in separating the MW and M31 components.

Recent work using moderate-resolution (Keck DEIMOS) multi-object spectroscopy of early-type supergiants led to the first detections of DIBs in M31 and M33 (Cordiner et al. 2008a, 2008b). Unusually large DIB equivalent widths per unit reddening (E_{B-V}), compared to the MW, were found in both galaxies. The λ5780 DIB was subsequently found to be strong relative to E_{B-V} in a sample of 17 sightlines in the vicinity of the M31 OB78 cluster (NGC 206; Cox & Cordiner 2008). However, these were selected from an observed set of 72 sightlines based on their strong DIBs relative to the spectral noise, so the results cannot be considered to be representative of the typical behavior of DIBs in M31. In addition, the blue spectra from Cox & Cordiner (2008) were of very poor quality, preventing the determination of precise stellar classifications and reddenings. In the present study, emphasis was placed on obtaining higher signal-to-noise spectra throughout the optical to facilitate the measurement of DIBs and the derivation of stellar spectral types.

In terms of its average gas-to-dust ratio (Nedialkov et al. 2000; Bresolin et al. 2002) and metallicity (e.g., Trundle et al. 2002), M31 has more in common with the MW than the MCs. However, there is strong evidence that the ISM in M31 is different from that of the MW and the MCs in the following ways: (1) the M31 star formation rate is presently about a tenth that of the MW (Walterbos & Braun 1994; Kang et al. 2009); (2) the ISRF is weak in the UV and devoid of far-UV radiation (e.g., Cesarsky et al. 1998; Pagani et al. 1999; Montalto et al. 2009)—interstellar dust grains have apparently not been subjected to the same degree of UV processing as in the MW (Cesarsky et al. 1998), which may explain the weakness of the mid-IR PAH bands in the center of M31; (3) the λ2175 Å UV extinction bump has been measured to be weak and narrow (Hutchings et al. 1992; Bianchi et al. 1996); (4) it has a narrow Serkowski polarization curve (Clayton et al. 2004), indicating a different grain-size distribution and/or dust-grain composition; and (5) the extinction law is peculiar as shown by the anomalously low average color-excess ratio E_{U-B}/E_{B-V} (Massey et al. 1995). Accepting the current theories of dust-grain extinction (reviewed by Draine 2003), evidence is consistent with a lack of small graphitic dust grains in the ISM of M31—a conclusion also reached by Xu & Helou (1994). Megier et al. (2001, 2005) identified correlations between Galactic DIB strengths and the shape of the UV extinction curve, which were interpreted as resulting from a physical or chemical relationship between the DIB carriers and the small grains responsible for extinction. Thus, it is of interest to examine whether differences in the size distribution of small grains in the M31 ISM compared to the MW give rise to any changes in the DIB spectrum.

Montalto et al. (2009) concluded, using UV and mid-IR maps of M31, that the observed dust emission is best represented by a model with high PAH abundances (>3% of available carbon) and a low UV field. In their scenario, dust is heated predominantly by an older stellar population, in agreement with the low mean intensity of the UV field. The relative lack of UV photons in M31 enables the examination of the hypothesis that a strong UV radiation field (on the level of that found in the MW ISM; e.g., Draine 1978) is required for DIB carrier production (see, for example, Herbig 1995 and Kendall et al. 2002).

In general, DIB equivalent widths (W) correlate well with E_{B-V} (e.g., Herbig 1993) and may therefore be used to estimate the amount of dust in a sightline. Thus, DIBs are becoming important as a measure of reddening in external galaxies and damped Lyman-alpha systems (see, for example, Lawton et al. 2008; Ellison et al. 2008), where they may be used to derive the best—and sometimes the only—estimate of E_{B-V}. Given the sparsity of DIB observations outside the MW, and the results of Cox et al. (2006), Welty et al. (2006), and Cordiner et al. (2008a, 2008b), which suggest that extragalactic DIBs may deviate from the MW E_{B-V} relationship, an important goal of our research is to examine the relationship between DIB equivalent widths and reddening in M31.

In this paper, we present the largest sample to-date of blue-to-red spectra of early-type supergiants in M31. Following the presentation of their spectral classifications and stellar radial velocities, we use these data to undertake the first survey of DIBs and interstellar Na I absorption lines across the disk of M31 and compare the properties and behavior of the DIBs with those measured in the MW.

2. TARGET SELECTION AND OBSERVATIONS

Early-type target stars were selected using *UBVRI* photometry from the Local Group Galaxies Survey (LGGS) catalog of 371,782 M31 stars (Massey et al. 2006). Photometric cuts of $V < 22$, $-0.45 \leqslant (B-V) \leqslant 0.45$, and $-1.2 \leqslant Q \leqslant -0.4$ (where the reddening-free Johnson Q-index is $Q = (U-B) - 0.72(B-V)$) were employed to select the brightest OB supergiants from the catalog. These cuts revealed a number of OB associations and star clusters across M31. To check the accuracy of the color cuts, stars in each association were cross matched with published spectral classifications (Massey et al. 1986, 1995) and our own unpublished, low-resolution spectra obtained using the *William Herschel Telescope*. Three fields were selected for observation using the Gemini Multi-Object Spectrograph (GMOS) on the Gemini North telescope, with the following parameters optimized: (1) the range of galactocentric distances (i.e., relative to the center of M31); (2) the number of previous OB-type classifications in the region; and (3) proximity to H II regions (the relationship between M31 stellar and H II region metallicities will be examined in a future paper). The three fields observed are in the fields numbered 3, 8, and 9 in the survey of Massey et al. (2006). Our Fields 2 and 3 (in Massey's Fields 8 and 3) include the OB78 and OB8 clusters, respectively (van den Bergh 1964). The three GMOS fields are shown in Figure 1 and cover regions in M31 with galactocentric distances of 14.4–18.4 kpc (Field 1), 8.9–9.6 kpc (Field 2), and ≈5.8 kpc (Field 3). The targets in each field were selected to optimize the number of apparently single B-type stars; any stars previously classified as

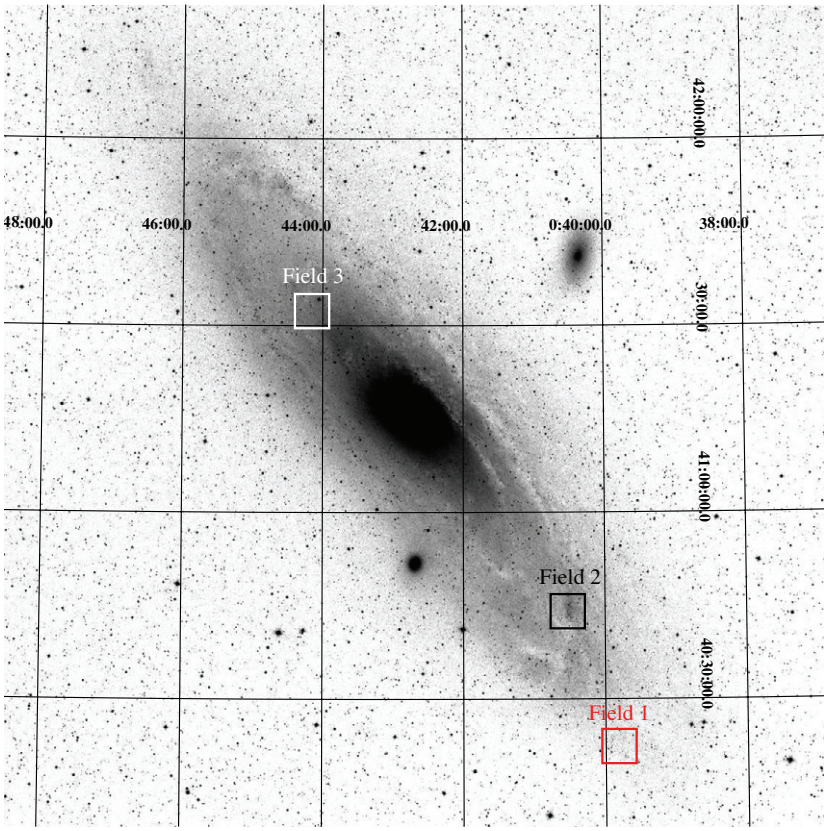

Figure 1. Optical image of M31 showing observed fields. Individual target locations are plotted in Figure 17. Credit: Bill Schoening, Vanessa Harvey/REU program/NOAO/AURA/NSF.

(A color version of this figure is available in the online journal.)

binaries, or which looked particularly asymmetric in the LGGS images, were excluded from the optimization routine. The orientation of each field was optimized to place the majority of stars in the center to ensure the optimal spectral coverage for each star. Coordinates and photometry for the final selection of 34 target stars are presented in Table 1.

Observations were carried out between 2007 August and 2008 January as part of queue-program GN-2007B-Q-116. Spectra were obtained in separate blue and red exposures, using the B1200 and R831 gratings, respectively, to obtain wavelength coverage from ∼4000 to 7000 Å. Using a slit width of 1″, the mean full width half-maximum (FWHM) of the calibration arc lines was 1.5 Å across the blue spectral range and 2.3 Å in the red. The resulting resolving power is variable as a function of wavelength and ranges from approximately 2500 in the blue to 3500 in the red. Seven or eight ∼30 minute exposures were obtained for each field in each wavelength range. Total integration times were as follows: Field 1: 3.9 hr (blue), 3.5 hr (red); Field 2: 4 hr (blue), 4.3 hr (red); and Field 3: 4 hr (blue), 3 hr (red).

The spectra were reduced using the IRAF `gemini.gmos` package.[10] Images were first cleaned of cosmic rays then flat fielded. Individual object images were wavelength calibrated and distortion-corrected using arc lamp exposures, then background-subtracted before extraction of the one-dimensional spectra. The wavelength calibration accuracy was confirmed by measuring the peak wavelengths of the Na D sky emission lines. Individual reduced spectra were velocity-corrected to the local standard of rest (LSR) frame before co-addition. The signal-to-noise per pixel (S/N) of the reduced spectra is typically ∼100 near the centers of the blue and red spectral ranges.

[10] IRAF is distributed by the National Optical Astronomy Observatory, which is operated by the Association of Universities for Research in Astronomy, Inc., under cooperative agreement with the National Science Foundation.

3. RESULTS

3.1. Stellar Classifications

Previous analyses of luminous B-type supergiants in M31 found abundances comparable to those in the solar neighborhood (e.g., Trundle et al. 2002). The GMOS spectra were therefore classified with respect to Galactic standards (Walborn & Fitzpatrick 1990; Lennon et al. 1992). Spectral types and stellar radial velocities are presented in Table 1; those stars with previous spectral classifications are listed for comparison with our new classifications in Table 2. Figure 2 shows a selection of the blue GMOS spectra, illustrating the spectral sequence of the B-type supergiants.

Reported stellar radial velocities are the mean measurements of the line centers of selected H, He, and metal absorption lines. The velocity for 4029.71 is a notable outlier of the Field 2 results and the spectrum shows some evidence for a potential second component (e.g., He II λ4200, although in the opposite velocity sense to what might be expected)—it seems likely this is a composite spectrum of more than one star.

Reddenings (E_{B-V}) were calculated using the intrinsic colors of Wegner (1994), supplemented by Johnson (1966) for later spectral types. The foreground reddening is discussed in Section 3.4.

Observational details of the 34 program stars are summarized in Table 1. We adopt abbreviated target names based on the

Table 1
Observed Target Star Details

Field	Abbr.	LGGS	V	$B-V$	Sp. Type	$v_{\rm LSR}$	E_{B-V}	$E_{B-V}^{\rm M31}$
1 (F9)	3936.51	J003936.51+402235.4	18.538	0.049	B5 Ia	−520 ± 2	0.13	0.07 ± 0.04
	3944.71[a]	J003944.71+402056.2	18.200	0.146	O9.7 Ib	−525 ± 5	0.38	0.32 ± 0.04
	3945.35	J003945.35+402115.4	17.933	0.325	B6 Ia	−505 ± 5	0.39	0.33 ± 0.04
	3945.82[a]	J003945.82+402303.2	18.480	−0.064	WN5 + O7	...	...	...
	3954.95	J003954.95+402405.4	18.728	0.014	B8 Ia	−551 ± 2	0.04	−0.02 ± 0.04
	3956.94[b]	J003956.94+402142.5	18.728	−0.137	B0.5 Ia	−518 ± 2	0.06	0.00 ± 0.04
	3958.22	J003958.22+402329.0	18.968	0.095	B0.7 Ia	−516 ± 2	0.30	0.24 ± 0.04
	3959.98	J003959.98+402221.1	18.625	−0.117	O9.7 Ib	−514 ± 4	0.11	0.05 ± 0.04
2 (OB78)	4026.74	J004026.74+404418.8	18.387	−0.071	B5 Ia	−579 ± 2	0.01	−0.05 ± 0.04
	4027.18	J004027.18+404233.2	18.009	−0.050	B3 Ia	−571 ± 2	0.03	−0.03 ± 0.04
	4029.57	J004029.57+404457.5	18.192	−0.020	B8 Ia	−590 ± 2	0.01	−0.05 ± 0.04
	4029.71	J004029.71+404429.8	18.561	−0.229	O7-7.5 Iaf	−651 ± 5	0.08	0.02 ± 0.04
	4030.28[a]	J004030.28+404233.1	17.357	−0.042	B1 Ia	−579 ± 3	0.15	0.09 ± 0.04
	4030.32[a]	J004030.32+404404.8	18.950	−0.063	B5 Ia	−578 ± 3	0.02	−0.04 ± 0.04
	4030.84	J004030.84+404348.6	18.827	−0.093	B2 Iab	−566 ± 3	0.07	0.01 ± 0.05
	4030.94	J004030.94+404246.9	18.866	−0.147	O9.5 Ib	−546 ± 5	0.09	0.09 ± 0.05
	4031.52[a]	J004031.52+404501.9	18.923	−0.147	B0.5 Ia	−591 ± 4	0.05	0.03 ± 0.05
	4032.28[a, b]	J004032.28+404506.7	17.916	−0.001	B8 Ia	−578 ± 4	0.03	−0.03 ± 0.04
	4032.88[a]	J004032.88+404509.9	17.952	−0.103	B2.5e	−590 ± 8	0.04	−0.02 ± 0.04
	4032.92	J004032.92+404257.7	18.193	−0.092	B0.5 Ia	−594 ± 2	0.11	0.05 ± 0.05
	4034.61	J004034.61+404326.1	18.669	0.150	B1 Ia	−561 ± 2	0.34	0.28 ± 0.04
	4034.68	J004034.68+404509.9	18.959	0.037	A0 Ia	−582 ± 3	0.03	−0.03 ± 0.04
	4034.80	J004034.80+404533.5	18.378	0.254	B8 Ia	−584 ± 2	0.28	0.22 ± 0.05
	4037.92	J004037.92+404333.3	18.657	0.056	B1.5 Ia	−571 ± 3	0.23	0.17 ± 0.04
3 (OB8)	4405.89[c]	J004405.89+413016.3	17.309	0.847	K0	...	0.03	...
	4406.87[b]	J004406.87+413152.1	19.019	−0.116	B1.5 Ia	−59 ± 4	0.05	−0.01 ± 0.04
	4408.04	J004408.04+413258.7	18.708	−0.017	B3 Ia	−105 ± 3	0.11	0.05 ± 0.04
	4408.36	J004408.36+413210.2	19.339	−0.098	B0.7 Ia	−104 ± 4	0.10	0.04 ± 0.05
	4408.79[a]	J004408.79+413142.0	19.602	−0.050	O8-9 II	−145 ± 1	0.24	0.18 ± 0.06
	4408.94	J004408.94+413201.2	18.356	−0.088	B1.5 Ia	−127 ± 5	0.08	0.02 ± 0.04
	4409.52	J004409.52+413358.9	19.302	−0.068	B2 Ib	−97 ± 4	0.12	0.06 ± 0.05
	4409.71[c]	J004409.71+413247.2	16.834	0.547	F8	...	0.00	...
	4412.17	J004412.17+413324.2	17.330	0.345	B2.5 Ia	−110 ± 5	0.49	0.43 ± 0.04
	4417.80[a]	J004417.80+413408.0	19.397	−0.055	O9.5 Ib	−94 ± 11	0.19	0.13 ± 0.05

Notes. LGGS designations and photometry are from Massey et al. (2006), abbreviated names used in this paper (Abbr.) are also given. Total line-of-sight reddenings (E_{B-V} in magnitudes) and radial velocities ($v_{\rm LSR}$ in km s^{-1}) are given. M31 reddenings ($E_{B-V}^{\rm M31}$) assume a foreground reddening of 0.06 mag as discussed in Section 3.4. Stars suffering from possible spectral and/or photometric contamination due to blending with nearby objects (as determined from the LGGS V-band images; Massey et al. 2006) are labeled "a". The spectrum of 3945.82 was kindly classified by Professor P. Crowther (2008, private communication). Two stars in Field 2 have negative $E_{B-V}^{\rm M31}$ values outside of the error bars, which may be indicative of a problem with their photometry, perhaps due to unseen multiplicity or variations in the assumed foreground reddening.

[a] Possibly blended with other objects.

[b] Stars used as telluric standards.

[c] Foreground stars.

Table 2
New Classifications Compared to Previous Work

Star	Alias	Sp. Type	Previous
3945.82	OB 135-1	WN5 + O7	WN[2]
4029.71	OB78-231	O7-7.5 Iaf	O8.5 I(f)[1]
4030.28	OB78-277	B1 Ia	B1.5 Ia[3]
4032.88	OB78-478	B2.5e	B1.5 Ia[4]
4032.92	OB78-485	B0.5 Ia	B0 I[5]
4037.92	...	B1.5 Ia	B0 I[6]
4406.87	OB8-7	B1.5 Ia	B1 I[1]
4408.36	OB8-25	B0.7 Ia	B1 I[1]
4408.94	OB8-34	B1.5 Ia	B1 Ia[1]
4409.52	OB10-43	B2 Ib	B8 Ia[1]
4412.17	...	B2.5 Ia	B5: I + H II[6]
4417.80	OB9-176	O9.5 Ib	Early B[1]

References. (1) Massey et al. 1995; (2) Massey et al. 1986; (3) Bianchi et al. 1994; (4) Trundle et al. 2002; (5) Humphreys et al. 1990; and (6) Massey et al. 2006.

minutes and seconds of right ascension in the LGGS catalog. Thus, stars belonging to each of the three fields are distinguished by the first two digits of their abbreviated names (39 for Field 1, 40 for Field 2, and 44 for Field 3).

3.2. DIB Sightlines

Of the stars observed, two are late-type foreground stars (4405.89 and 4409.71) and one (3945.82) is a Wolf–Rayet in M31, and therefore unsuitable for our DIB survey. To investigate the DIBs in M31, only the sightlines passing through a significant quantity of ISM were selected for further analysis. Each spectrum was examined for the presence of DIBs, by reference to the survey of Hobbs et al. (2008). No DIBs were detected toward stars with a foreground-corrected reddening of $E_{B-V}^{\rm M31} < 0.05$ mag. This is as expected given the spectral noise, and the assumption that M31 DIB strengths are similar to those typically observed in the MW: for the typical S/N of the spectra near 5780 and 6283 Å (100 and 80, respectively), using the

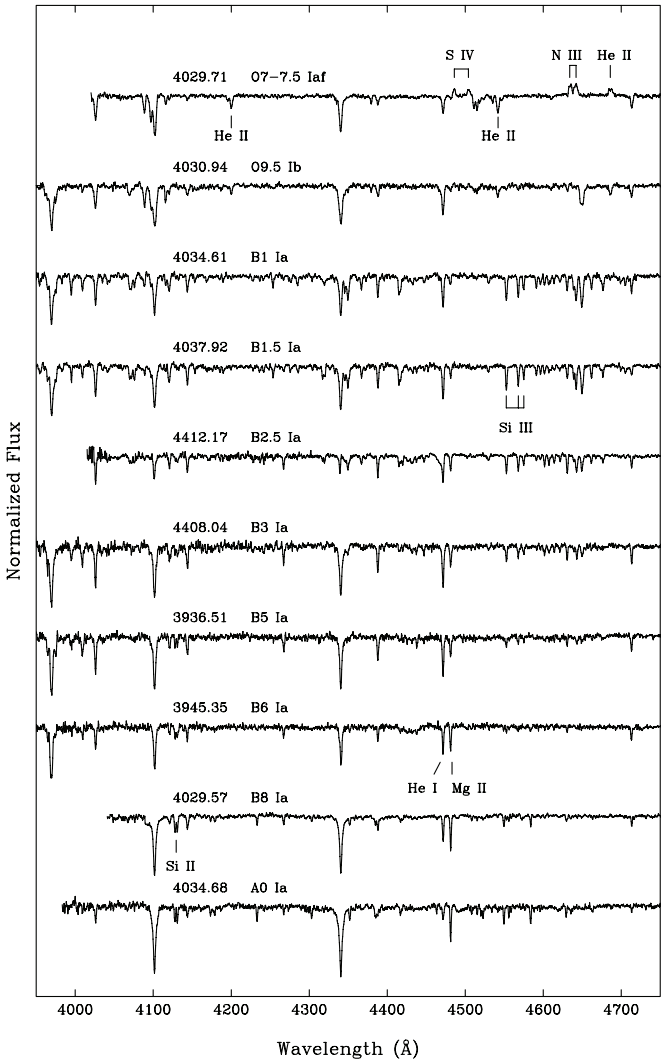

Figure 2. Montage of observed M31 supergiants over the range of spectral types O7 Iaf to A0 Ia. Note the trends in the primary diagnostic lines: He I λ4471, He II λλ4200, 4541, 4686, Mg II λ4481, Si II λλ4128, 4130, and Si III λλ4552, 4560, 4574. Also labeled in the spectrum of 4029.71 are the S IV, N III, and He II emission lines.

approximate minimum DIB W detection threshold equation of Hobbs et al. (2008; $W_{\rm max} = 1.064\times$ FWHM/(S/N)) yields respective lower detection limits of 22 and 63 mÅ for these DIBs. Scaled to a reddening of $E_{B-V} = 0.04$, the mean Galactic λλ5780 and 6283 DIB W/E_{B-V} values are 21 and 47 mÅ, respectively (using data from Herbig 1993, Thorburn et al. 2003, Megier et al. 2005, and Cordiner 2006), which is consistent with their non-detection in our spectra at M31 reddenings of 0.04 and less. The sample of 14 stars with $E^{\rm M31}_{B-V} \geqslant 0.05$ is listed in Table 3, with the addition of three targets (3956.94, 4032.28, and 4406.87), which were used as telluric standards for Fields 1, 2, and 3, respectively.

3.3. Sodium D Lines: Column Densities and Radial Velocities

Sky-subtracted spectra of the regions covering the sodium D lines are shown in Figure 3. At the resolution of the GMOS spectra (100 km s^{-1} in this wavelength region), the interstellar Na D absorption lines in M31 and the MW can be modeled using single Gaussian interstellar cloud components. Both lines of the Na D doublet were fitted simultaneously using the VAPID routine (Howarth et al. 2002) to produce models of the Galactic and M31 Na I distributions in each sightline. Fitting both lines of the sodium doublet simultaneously helps to constrain the Doppler b parameter in data at this relatively low spectral resolution. The resulting interstellar Na I cloud radial velocities, Doppler b parameters, and column densities are summarized in Table 3. Monte Carlo error estimates were generated by refitting each cloud model to 100 different replicated spectra, each with random Poisson noise added, and taking the ±68th percentiles of the resulting (free) parameter ranges.

The Doppler shift of Field 3 is comparable to the instrumental resolving power, and as a result, the MW and M31 absorption components are blended which hinders the accurate derivation of the individual component parameters. To obtain physically realistic results for 4409.52 and 4412.17, the velocity and Doppler b parameter of the MW component had to be held fixed during the fitting (at $v = -23.3$ km s^{-1} and $b = 19.9$ km s^{-1}, which are the averages for the MW components toward the other stars in Table 3). Toward the telluric standard 4406.87, there was no detectable M31 component of Na I; the only absorption detected is at a mean radial velocity of $-32.0^{+5.2}_{-4.2}$ km s^{-1} which is unlikely to be in M31 and is consistent (in velocity and column density) with the other MW foreground components observed toward the stars in Fields 1 and 2. An upper limit on the M31 Na I column density of 2.8×10^{11} cm^{-2} was derived for this sightline assuming the radial velocity and Doppler width of the gas to be the average of those values measured toward the other stars in Field 3. It must be noted, however, that all of the Field 3 Na I fit parameters are subject to additional uncertainty due to the likely contamination of the spectra by sky-subtraction residuals. Strong telluric Na I emission features dominate these GMOS spectra at velocities ±100 km s^{-1} with respect to the D-line centers, and their imperfect subtraction during data reduction thus leads to potential uncertainties in the spectra over this velocity range.

The observed sightlines pass through the halo of M31 and are expected to intercept multiple interstellar clouds with component structure that is unresolved in our spectra. Thus, the derived (single-component) interstellar cloud models provide no information about the detailed kinematics of the M31 ISM except for the overall velocity width and peak radial velocity of the Na I gas distributions. The column densities derived from these broad, single-component fits should generally be considered as lower limits due to the likely presence of unresolved saturated structure in the Na D lines.

Since sodium lines can be present in the background stellar spectra, we investigated the possible stellar Na D contributions to our observed spectra. Theoretical spectra for a range of stellar types spanning those observed were calculated using SYNSPEC (Hubeny & Lanz 2000) and Kurucz (1993) model atmospheres with solar metallicity. Stellar contributions to the Na D line equivalent widths were found to be negligible compared with the interstellar component for all the stars listed in Table 3; only in cooler stars (of type A and later) does the stellar contribution become important.

The measured M31 interstellar sodium radial velocities match the velocities of nearby M31 stars and planetary nebulae, as can be seen in Figure 4. This demonstrates with little ambiguity that these clouds are located in the main disk of M31.

3.4. Foreground Reddening and DIBs in the Galactic Halo

The mean foreground Na I column density toward our surveyed M31 stars is 3.2×10^{12} cm^{-2}. Sembach et al. (1993) measured the Na I column density in lines of sight through the

Table 3
Best-fit Interstellar Na I Cloud Model Parameters for the Galactic (MW) and M31 ISM

Sightline	MW			M31		
	v	b	N	v	b	N
3936.51	$-0.4^{+4.1}_{-5.6}$	$4.8^{+3.7}_{-1.7}$	$12.43^{+0.28}_{-0.22}$	$-526.0^{+2.4}_{-3.0}$	$7.9^{+1.2}_{-1.1}$	$12.90^{+0.14}_{-0.13}$
3944.71	$11.5^{+5.8}_{-6.2}$	$10.4^{+37.9}_{-7.5}$	$12.14^{+0.18}_{-0.15}$	$-518.5^{+1.0}_{-1.2}$	$10.5^{+1.6}_{-1.5}$	$13.57^{+0.38}_{-0.29}$
3945.35	$-4.55^{+3.9}_{-6.9}$	$49.4^{+11.9}_{-13.9}$	$12.09^{+0.03}_{-0.04}$	$-514.0^{+1.1}_{-1.1}$	$11.1^{+1.0}_{-0.9}$	$13.16^{+0.11}_{-0.10}$
3956.94[b]	$-46^{+4.6}_{-5.5}$	$3.8^{+1.4}_{-0.9}$	$12.77^{+0.45}_{-0.27}$	$-521.4^{+7.8}_{-8.1}$	$3.7^{+3.1}_{-1.9}$	$12.36^{+0.56}_{-0.33}$
3958.22	$-45.6^{+7.8}_{-7.8}$	$5.2^{+2.4}_{-2.1}$	$12.79^{+0.69}_{-0.26}$	$-516.6^{+4.1}_{-4.6}$	$7.0^{+2.2}_{-1.4}$	$13.29^{+0.45}_{-0.41}$
3959.98	$-41.2^{+4.8}_{-6.5}$	$5.9^{+3.9}_{-2.0}$	$12.47^{+0.27}_{-0.18}$	$-502.5^{+3.7}_{-4.7}$	$3.0^{+0.4}_{-0.4}$	$13.56^{+0.63}_{-0.42}$
4030.28	$-2.0^{+3.0}_{-3.8}$	$51.3^{+7.3}_{-7.0}$	$12.33^{+0.03}_{-0.02}$	$-578.5^{+3.8}_{-5.1}$	$46.8^{+7.3}_{-10.6}$	$12.24^{+0.03}_{-0.03}$
4032.28[b]	$-34.1^{+3.0}_{-3.2}$	$10.2^{+5.3}_{-2.8}$	$12.58^{+0.09}_{-0.11}$	$-571.7^{+22.5}_{-16.3}$	$58.2^{+29.6}_{-40.5}$	$11.79^{+0.12}_{-0.10}$
4034.61	$-35.7^{+5.4}_{-6.3}$	$8.5^{+21.1}_{-6.3}$	$12.41^{+0.24}_{-0.19}$	$-552.2^{+2.8}_{-2.8}$	$62.2^{+6.9}_{-6.6}$	$12.78^{+0.02}_{-0.02}$
4034.80	$-49.6^{+3.5}_{-3.7}$	$26.0^{+8.9}_{-10.2}$	$12.50^{+0.04}_{-0.03}$	$-548.8^{+2.8}_{-2.6}$	$11.6^{+42.6}_{-2.3}$	$13.08^{+0.22}_{-0.35}$
4037.92	$-29.8^{+4.9}_{-7.4}$	$49.7^{+13.8}_{-15.2}$	$12.31^{+0.04}_{-0.04}$	$-554.2^{+3.1}_{-3.6}$	$7.4^{+2.0}_{-1.6}$	$13.26^{+0.51}_{-0.35}$
4406.87[b]	$-34.0^{+3.2}_{-3.5}$	$16.9^{+7.5}_{-6.0}$	$12.34^{+0.04}_{-0.03}$	-121.0[a]	12.0[a]	< 11.4
4408.04	$-32.0^{+5.2}_{-4.2}$	$22.7^{+10.2}_{-11.0}$	$12.55^{+0.12}_{-0.05}$	$-151.3^{+2.0}_{-1.9}$	$10.9^{+1.9}_{-2.7}$	$13.48^{+0.62}_{-0.24}$
4408.79	$4.4^{+10.2}_{-11.6}$	$10.5^{+15.5}_{-5.6}$	$12.81^{+0.49}_{-0.24}$	$-90.5^{+10.7}_{-13.2}$	$7.7^{+3.2}_{-3.5}$	$13.10^{+0.95}_{-0.36}$
4409.52	-23.2[a]	19.9[a]	$12.43^{+0.05}_{-0.06}$	$-119.2^{+2.5}_{-2.2}$	$16.2^{+2.6}_{-3.0}$	$13.16^{+0.18}_{-0.10}$
4412.17	-23.2[a]	19.9[a]	$12.28^{+0.20}_{-0.24}$	$-122.9^{+0.7}_{-0.7}$	$18.5^{+0.9}_{-1.1}$	$13.25^{+0.05}_{-0.03}$
4417.80	$-40.4^{+6.0}_{-6.4}$	$23.4^{+9.4}_{-6.0}$	$12.60^{+0.12}_{-0.05}$	$-121.1^{+5.3}_{-8.3}$	$7.5^{+1.6}_{-2.4}$	$13.22^{+0.47}_{-0.27}$

Notes. Radial LSR velocities (v) and Doppler b parameters are in km s^{-1}. Column densities (N) are in log cm^{-2}. Statistical Monte Carlo errors are given. The MW model parameters may be uncertain due to contamination of the Na D lines near $v = 0$ by sky-subtraction residuals. M31 column densities should generally be considered as lower limits due to the likely presence of unresolved saturated structure in the Na D lines.
[a] Values held fixed during the fitting.
[b] Telluric standard stars.

Galactic halo, probing gas that should be similar to the MW foreground ISM in our sightlines. The correlation between Na I and E_{B-V} permits an estimate of the foreground reddening. Performing a least-squares fit to the Sembach et al. (1993) data yields a linear relationship: $E_{B-V} = (N(\mathrm{NaI}) + 1.41 \times 10^{11})/3.79 \times 10^{13}$, from which we derive a foreground reddening of $E_{B-V} = 0.088$ mag. However, there is considerable scatter in the Na I versus E_{B-V} data—the mean rms error on E_{B-V} is 0.053—and there is likely to be contamination of our Na I profiles near $v = 0$ due to sky-line subtraction residuals. These factors make the derivation of foreground reddening from Na I quite uncertain. From the Leiden/Argentine/Bonn (LAB) H I survey[11] (Kalberla et al. 2005; Hartmann & Burton 1997), the spectra obtained at the points nearest the centers of our three fields give foreground H I column densities of 5.75×10^{20} cm^{-2} (Field 1), 6.07×10^{20} cm^{-2} (Field 2), and 6.68×10^{20} cm^{-2} (Field 3), assuming optically thin emission. Using Equation (7) of Burstein & Heiles (1978) (which assumes a constant gas-to-dust ratio) to calculate the foreground reddening, the average value is $E_{B-V} = 0.068$ mag. The modified Burstein & Heiles relation utilized by the NED database[12] results in $E_{B-V} = 0.0625$ mag, which is in good agreement with the foreground reddening toward M31 estimated by Schlegel et al. (1998) from the median Galactic dust emission in the surrounding regions ($E_{B-V} = 0.062$ mag). We therefore adopt an MW foreground reddening of 0.06 ± 0.02, which is used in the calculation of the foreground-corrected reddenings (E^{M31}_{B-V}) given in Table 1. Quoted errors on E^{M31}_{B-V} include an uncertainty of 0.02 in the foreground reddening, plus the uncertainty on the intrinsic stellar $B-V$ values (equal to the uncertainty of a single spectral subclass).

As shown in Figure 5, the λ5780 DIB is detected in several of the observed sightlines at a wavelength matching the Galactic λ5780 rest wavelength of 5780.37 Å (see, for example, Galazutdinov et al. 2000). This absorption feature most likely originates in the Galactic halo. The average foreground λ5780 equivalent width is 40 ± 10 mÅ, as measured from the co-added spectrum of all the stars from Fields 1 and 2 listed in Table 1 (excluding the Wolf–Rayet and those sightlines in Field 3 with blended MW and M31 Na I cloud components). Using a Gaussian fit, the mean radial velocity of the λ5780 carrier gas was found to be 0.5 ± 7.3 km s^{-1}. The mean Galactic λ5780 equivalent width per unit reddening is $[W(5780)/E_{B-V}]_{\mathrm{mean}} = 527$ mÅ mag^{-1}, with a standard deviation of 230 mÅ mag^{-1} (see Section 3.2 for details of the literature data used; the outliers toward ρ Oph and the Orion Nebula have been excluded). Using this ratio, the average MW foreground λ5780 equivalent width measured toward M31 corresponds to a foreground reddening of $E_{B-V} = 0.08^{+0.08}_{-0.04}$ mag, which is consistent with the value of 0.06 adopted in this study.

3.5. M31 Diffuse Interstellar Bands: Equivalent Widths and Radial Velocities

We searched the spectra of each of the sightlines with foreground-corrected reddening $E^{\mathrm{M31}}_{B-V} \geqslant 0.05$ for the DIBs listed in the survey of Hobbs et al. (2008). For the λλ6283 and 6993 DIBs, which are partially obscured by overlapping telluric lines, corrections were performed by division with spectra from lines of sight with negligible E^{M31}_{B-V} selected from the same field (designated with superscript "b" in Table 1). The λλ4428, 5705,

[11] http://www.astro.uni-bonn.de/~webrai/english/tools_labsurvey.php
[12] The NASA/IPAC Extragalactic Database (NED) is operated by the Jet Propulsion Laboratory, California Institute of Technology, under contract with the National Aeronautics and Space Administration.

5780, 5797, 6203, 6269, 6283, 6379, 6613, 6660, and 6993 DIBs were detected in at least one sightline each, with Doppler shifts matching the M31 Na I and H I velocities (H I data are presented in Section 3.6). The λ5849 and λ6445 DIBs were tentatively detected in the spectrum of 3944.71 only. The λλ4501, 4726, 6196, 6376, and 6532 DIBs were too weak to be detected in any of the spectra, which is consistent with the assumption of MW-like strengths (per unit reddening), given the S/N and low resolving power of our spectra. Severe contamination by telluric absorption prevented analysis of the λλ6886, 6919, 7224, and 7334 DIBs. Equivalent widths were measured by integration across a linear- or quadratic-fitted continuum. Errors on DIB equivalent widths measured this way were determined by $\sigma\Delta\lambda$, where σ is the rms noise in the continuum and $\Delta\lambda$ is the FWHM of each DIB. As a result of the relatively low S/N and low dispersion of the spectra compared with other contemporary Galactic DIB studies (e.g., McCall et al. 2010), additional uncertainties in the measured DIB equivalent widths arise due to the difficulties in establishing the true full widths of the DIBs over which to perform the integration. For example, in Figure 5 the presence of overlapping weak stellar/noise features at the wings of the λ5780 DIB observed toward 3944.71, 4034.80, and 4412.17 causes depressions in the continua that cannot be distinguished from the DIB by eye, and thus artificially boost the measured equivalent widths. Conversely, the broad, shallow, Lorentzian-like wings of the λ6283 DIB (shown in Figure 6) are lost in the noise, resulting in likely underestimation of the full width of this feature. Therefore, to provide a second, more accurate measurement of the λλ5780 and 6283 radial velocities and equivalent widths that takes the complex profiles of the DIBs into account, Galactic DIB template spectra were fitted to the observed M31 spectra.

The Galactic DIB templates were derived from high-resolution ($R = 58{,}000$), high S/N (~ 2000) spectra of β^1 Sco (see Cordiner 2006), shifted to the interstellar rest frame. These were convolved with a Gaussian interstellar cloud model, then with the GMOS spectral point spread function (assumed Gaussian), and rebinned to the dispersion of the GMOS spectra. The interstellar cloud model was optimized using the same nonlinear least-squares algorithm employed by the VAPID code (Howarth et al. 2002). This technique has the benefit that the statistical uncertainties in the measurements of the equivalent widths and velocities of weak DIBs are minimized, but has the drawback that the intrinsic M31 DIB profiles and rest wavelengths are assumed to closely match those of the MW DIB standard star β^1 Sco. If this were not the case, unknown systematic errors could occur, but there is no evidence to suggest that M31 DIB profiles differ from those of β^1 Sco. Profiles of some Galactic DIBs have been shown to exhibit variations in substructure (Galazutdinov et al. 2002). So far, however, all observed variations have been small and are negligible compared to the size of the GMOS resolution element and the level of noise in our spectra. The reader is referred to Section 3.5.2 of Cordiner (2006) for a more detailed discussion of the merits of the DIB fitting technique.

The fitted and integrated equivalent widths are shown in Table 5 and match each other to within the error bars. However, for four out of seven cases (for which the DIBs are not affected by obvious blends, denoted by superscript *b*), the fitted values of $W(5780)$ are systematically less than the integrated values. For $W(6283)$, the fitted values are generally greater than the integrated values. These differences are as expected given the increased accuracy afforded by using known DIB profiles to better constrain their full widths, as explained above.

Error estimates for the λ5780 and λ6283 equivalent widths and velocities were derived by the same Monte Carlo technique as used for the Na I spectral modeling; 500 different replicated spectra were produced for each DIB with (random) Poisson noise added to each, the σ value which was taken to be equal to the rms noise of the local continuum. Errors due to the uncertainties inherent in the spectral continuum rectification were accounted for by multiplicatively scaling each replicated spectrum by a random factor of between $1-\sigma$ and $1+\sigma$. The DIB model parameters were refitted for each replicated spectrum and individual parameter errors were obtained from the ±68th percentiles of the respective parameter ranges.

As can be seen from the data in Table 4, the error estimates on the DIB equivalent widths derived from Monte Carlo fitting (in the column labeled as "Fit.") are typically larger (by $\sim$ 50%) than those derived using $\sigma\Delta\lambda$ (column labeled as "Int."). Although our Monte Carlo errors do not take account of interloping stellar features (these are considered separately; see below), they are expected to be more reliable than the $\sigma\Delta\lambda$ errors, which assume a somewhat arbitrary $\pm 1\sigma$ error on the continuum placement, as described by McCall et al. (2010), and do not take into account the non-Gaussianity of the DIB profiles, which is especially important for λ6283 with its very broad, Lorentzian-like wings.

The spectral regions spanning the λ5780 and λ5797 DIBs are shown in Figure 5 for the 14 stars in our M31 reddened sample (plus three telluric standards). The spectral regions covering λ6269 and λ6283 are shown in Figure 6 (these spectra have been divided by the spectra of the telluric standards from each respective field). M31 components of λ5780 are detected in 9 sightlines and λ6283 in 11 sightlines. The MW foreground λ6283 components are effectively removed during telluric division because of their presence in the telluric standard spectra.

A total of 11 different DIBs (λλ4428, 5705, 5780, 5797, 6203, 6269, 6283, 6379, 6613, 6660, and 6993) were detected in M31 toward the three most reddened targets 3944.71, 3945.35, and 4412.17 (data presented in Table 5 and Figures 5–13). Figures 8–13 also show reference MW DIB spectra (from Cordiner 2006), as well as telluric standard spectra to illustrate the likely level of contamination by stellar and telluric features.

To account for possible additional uncertainties in the DIB equivalent widths given in Table 5 due to the presence of overlapping stellar lines, we have estimated the possible stellar line contributions. The table shows the total equivalent widths of stellar features that might be overlapping the DIBs, calculated from synthetic B0 Ia and B9 Ia stellar spectra (at temperatures of 28,000 and 10,000 K, respectively), using the method described in Section 3.3. The line list used in the spectral modeling includes transitions of the following elements and their ions: H, He, C, N, O, Na, Mg, Si, Ca, Cr, Mn, and Fe. The calculated stellar line contributions to measured DIB equivalent widths are generally small (except for the very broad λ4428 DIB which is contaminated by the O II blend near 4415 Å) and in most cases are negligible compared with the errors arising from continuum placement and statistical noise.

As a result of the close blending between the MW and M31, interstellar gas components due to the low Doppler shift of Field 3 (discussed further in Sections 3.3 and 3.6), there may be some ambiguity as to which galaxy the Field 3 DIBs originate. The main discriminator we use to identify the location of the DIB carriers is their radial velocity compared with the Na I component structure. The separation of the MW and M31 DIB

velocities is clear in all cases apart from 4412.17 and 4417.80, for which the DIB velocities appear to be intermediate between the M31 and MW Na I components. However, a number of factors lead us to conclude that the DIBs observed in these sightlines originate in M31: (1) the DIB velocities match the peak M31 H I velocities (see Section 3.6), whereas we detect a negligible contribution to the DIB equivalent widths at radial velocities corresponding to H I in the MW (at $v_{\rm LSR} < 45$ km s^{-1}; see Braun et al. 2009); (2) LAB survey data toward the targets in question (Kalberla et al. 2005; Hartmann & Burton 1997) show a relatively small foreground H I component, such that the $W(5780)/N(\rm H\,I)$ ratios toward 4412.17 and 4417.80 would be very large if this DIB originated in the MW halo and inconsistent with the values observed previously in the MW ISM (see Figure 8 of McCall et al. 2010); (3) assuming the Galactic halo obeys the average MW DIB W versus E_{B-V} relation, the equivalent widths expected from the M31 foreground reddening of $E_{B-V} = 0.06 \pm 0.02$ are only 32 ± 11 mÅ for λ5780 and 71 ± 24 mÅ for λ6283, whereas the measured DIB equivalent widths toward 4412.17 of 190 ± 17 mÅ and 491 ± 82 mÅ, respectively, are consistent with the M31 reddening ($E^{\rm M31}_{B-V}$) in this sightline; and (4) the Na I spectrum of 4406.87 in Figure 3, which shows no evidence for M31 Na I absorption, gives another indication of the properties of the foreground (MW) neutral gas in Field 3. The quantity and velocity of this foreground gas are very similar to the amount of gas in the other fields where the MW λ5780 components (which can be easily separated from the M31 DIBs) are clearly very weak. Assuming the foreground gas chemical properties are not grossly variable on the scale of the $\sim 1^\circ$ that separates the GMOS fields, this strongly suggests that the foreground DIBs in Field 3 would be similarly as weak. Small-scale structure in the Galactic halo could produce variations in the relative abundances of atoms, dust, and DIB carriers, but given the reasons outlined above, it is highly unlikely that the Field 3 DIBs originate in chemically peculiar, compact, high-velocity Galactic clouds.

3.6. H I 21 cm Emission and the M31 Gas-to-Dust Ratio

Dr. Robert Braun kindly made available data cubes and opacity-corrected H I column density maps from the Braun et al. (2009) 21 cm survey of M31, performed using the Westerbork Synthesis Radio Telescope and the Green Bank Telescope. These data are at a spatial resolution of $18'' \times 15''$, which corresponds to a linear resolution of 70×56 pc at the distance of M31. The H I spectra have a velocity resolution of 2.3 km s^{-1}. From these data, we used bi-linear interpolation to extract opacity-corrected column densities and H I spectra for our targets (shown in Figure 14).

Opacity-corrected H I column densities and gas-to-dust ratios $G = \frac{1}{2} N(\rm H\,I)/E^{\rm M31}_{B-V}$ are given in Table 4; the gas-to-dust ratio has thus been calculated assuming that half of the total H I column lies in front of the target stars. However, this fraction is uncertain, so the errors on G are ±100%.

The average gas-to-dust ratios are 13.4, 8.2, and 7.7 (in units of 10^{21} cm^{-2} mag^{-1}), for Fields 1–3, respectively, with an overall average of 9.8. Previous measurements of the M31 gas-to-dust ratio lie in the range $\approx$ (5–15) $\times 10^{21}$ cm^{-2} mag^{-1} (van den Bergh 1975; Bajaja & Gergely 1977; Kumar 1979; Lequeux 2000). These values may be compared with the nearby Galactic value of 5.8×10^{21} cm^{-2} mag^{-1} (Bohlin et al. 1978), which was derived from H I absorption lines and therefore does not suffer from the problem of background contamination. It is difficult to draw firm conclusions from these data due to the uncertainties in

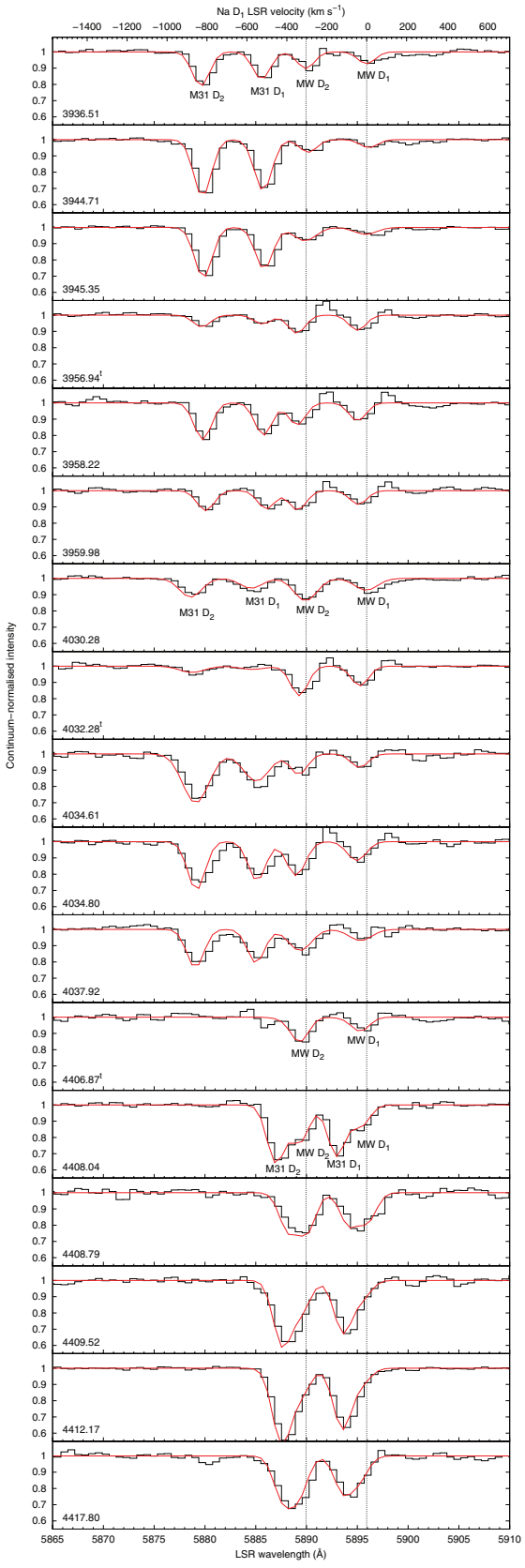

Figure 3. Observed continuum-normalized Na I spectra (histograms) with best-fitting interstellar cloud models overlaid. The velocity scale at the top is relative to the Na D_1 rest wavelength. Stellar He λ5876 lines have been removed from the observed spectra using Gaussian fits. MW and M31 absorption components are marked. Dotted lines show the Na D rest wavelengths. The superscript "t" denotes stars used as telluric standards.

(A color version of this figure is available in the online journal.)

Table 4

λ5780 and λ6283 DIB Equivalent Widths and Velocities, M31 H I 21 cm Column Densities, Gas-to-dust Ratios, Interstellar NUV Radiation Field Strengths, and *Spitzer* 8/24 μm Flux Ratios for Observed Sightlines

Sightline	W(5780)		W(6283)									
	Fit (mÅ)	Int. (mÅ)	Fit (mÅ)	Int. (mÅ)	v(5780) (km s^{-1})	v(6283) (km s^{-1})	N(H I) (10^{21} cm)$^{-2}$	G (10^{21} cm^{-2} mag^{-1})	$I_{\rm NUV}$ Draine	8/24 μm Flux	$W(5780)/E_{B-V}$ (Å mag^{-1})	$W(6283)/E_{B-V}$ (Å mag^{-1})
3936.51	84^{+33}_{-32}	89 (19)	279^{+96}_{-85}	217 (55)	$-510.7^{+36.8}_{-36.0}$	$-498.5^{+63.9}_{-49.3}$	2.8	20	0.27	1.16	$1.2^{+2.8}_{-0.7}$	$4.0^{+8.9}_{-2.3}$
3944.71	318^{+26}_{-24}	359 (17)	671^{+79}_{-71}	544 (48)	$-512.4^{+7.5}_{-7.0}$	$-524.8^{+13.6}_{-15}$	4.5	7.1	0.48	0.63	$1.0^{+0.2}_{-0.2}$	$2.1^{+0.6}_{-0.4}$
3945.35	202^{+22}_{-24} [a]	302 (14)[a]	587^{+69}_{-74}	414 (52)	$-515.4^{+12.2}_{-11.7}$	$-510.6^{+15.6}_{-15.4}$	4.2	6.4	0.35	0.94	$0.6^{+0.2}_{-0.1}$	$1.8^{+0.5}_{-0.4}$
3958.22	211^{+33}_{-48}	207 (35)	439^{+98}_{-89}	419 (60)	$-517.9^{+18.1}_{-16.7}$	$-511.9^{+26.4}_{-25.4}$	4.0	8.5	0.35	1.78	$0.9^{+0.4}_{-0.3}$	$1.9^{+0.9}_{-0.6}$
3959.98	<29	<42	117^{+90}_{-60}	124 (54)	...	$-481.3^{+81.6}_{-51.6}$	2.6	25	0.59	0.71	<2.2	$2.2^{+13.8}_{-1.6}$
4030.28	<41	<28	<42	<112	...	...	2.8	16	3.1	0.90	<0.9	<0.9
4034.61	120^{+39}_{-41}	165 (25)	375^{+105}_{-89}	405 (65)	$-514.9^{+33.3}_{-35}$	$-601.3^{+31.0}_{-30.4}$	2.3	4.0	2.9	1.20	$0.4^{+0.2}_{-0.2}$	$1.3^{+0.7}_{-0.4}$
4034.80	215^{+24}_{-26}	238 (22)	383^{+76}_{-78}	326 (54)	$-584.5^{+14.2}_{-13.7}$	$-543.5^{+25.3}_{-27.4}$	1.3	2.9	1.9	1.15	$1.0^{+0.4}_{-0.3}$	$1.7^{+0.9}_{-0.6}$
4037.92	<39	<49	177^{+122}_{-82}	123 (68)	...	$-600.1^{+43.4}_{-49.1}$	3.3	10	0.97	1.38	<0.3	$1.1^{+1.3}_{-0.6}$
4408.04	<30	<40	<243	<142	...	...	1.6	15	0.79	1.16	<2.3	<2.7
4408.79	146^{+74}_{-48} [a]	<88	189^{+169}_{-115}	171 (104)	...	$-93.8^{+39.0}_{-47.0}$	1.2	3.4	0.83	1.05	$0.8^{+1.0}_{-0.4}$	$1.1^{+1.9}_{-0.7}$
4409.52	<38	<57	<65	<168	...	...	1.4	11	0.59	1.26	<3.2	<5.4
4412.17	190^{+17}_{-16}	256 (10)	491^{+83}_{-81}	423 (53)	$-88.1^{+8.2}_{-8.2}$	$-82.8^{+17.7}_{-22.3}$	2.0	2.3	1.1	0.90	$0.8^{+1.0}_{-0.4}$	$1.1^{+1.9}_{-0.7}$
4417.80	79^{+55}_{-41}	<57	194^{+148}_{-92}	221 (76)	$-99.3^{+57.8}_{-48.6}$	$-107.0^{+42.3}_{-55.6}$	1.7	6.6	0.48	0.76	$0.6^{+1.2}_{-0.4}$	$1.6^{+3.0}_{-1.0}$

Notes. Fitted and continuum-integrated DIB equivalent widths are given, labeled Fit. and Int., respectively. The errors (±) on the integrated equivalent widths are $\sigma\Delta\lambda$ and are given in brackets, with upper limits calculated as $2\sigma\Delta\lambda$. Errors on the gas-to-dust ratios ($G = \frac{1}{2}\ N(\mathrm{H\,I})/E^{\mathrm{M31}}_{B-V}$) are ±100% due to probable contamination by background H I (see Section 3.6).

[a] DIB equivalent widths probably affected by line blending.

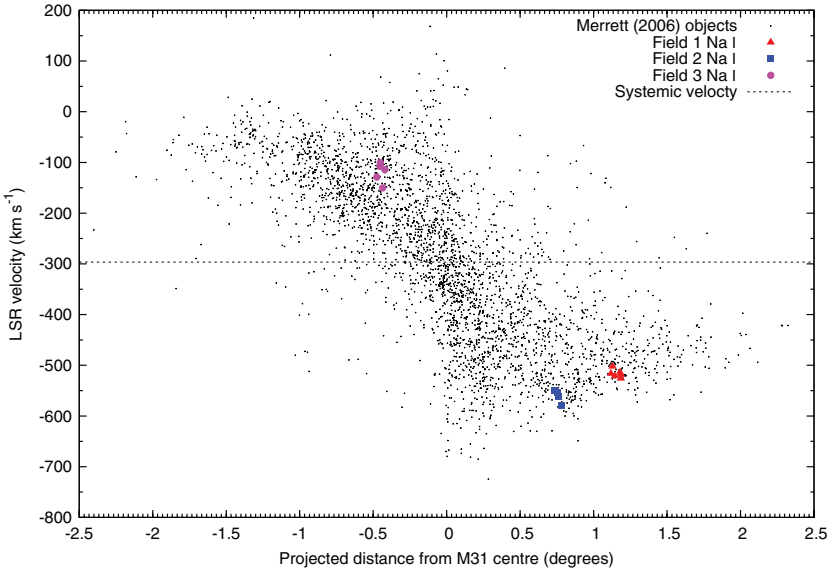

Figure 4. Kinematic (position–velocity) map of M31 along the galaxy's major axis, showing the emission-line objects (mostly planetary nebulae) from the survey by Merrett et al. (2006) and our measured interstellar Na I velocities. Data points for each GMOS field are plotted using a different symbol.
(A color version of this figure is available in the online journal.)

the fraction of background H I in M31, but it seems reasonable to conclude that the gas-to-dust ratio of M31 is broadly similar to that of the MW. Although many of the observed sightlines appear to have gas-to-dust ratios significantly greater than Galactic, this may be caused by an observational bias toward stars located on the near side of the M31 disk; our derived gas-to-dust ratio would be an overestimate in such cases. Accounting for errors, the gas-to-dust ratio is lower toward 4412.17 than the average MW value. This sightline also clearly exhibits relatively weak DIBs per unit reddening.

Figure 14 shows that the velocities of the interstellar clouds as probed using Na I lines correspond imperfectly with the peak H I velocity in many cases. This may be due to the presence of background H I clouds that do not contribute to the Na I absorption spectra. However, for three of the Field 3 stars, the Na I velocities do not match the H I gas at all, with Na I velocities at least 20 km s^{-1} redward of the H I. For 4412.17 and 4417.80, the Na I velocities are similarly displaced from the DIB velocities (see Section 3.5), but the DIBs match very closely with the positions of the H I peak velocities. Given that DIB carriers, Na I and H I are correlated (e.g., Hobbs 1974; Ferlet et al. 1985; Herbig 1993; McCall et al. 2010), and their velocities are generally closely matched in the diffuse ISM, there is likely to be a problem with the measured M31 Na I cloud velocities in Field 3 (probably for the reasons related to sky subtraction discussed in Section 3.3). The measured Na I velocities would be offset to the red (as observed) if the MW component is not as strong as was derived in the VAPID model fits or if the sky-line subtraction was incomplete. To resolve this situation would require high-resolution Na I spectra in order to separate the M31 and MW components. The H I gas in Field 3 spans a relatively narrow range of radial velocities (from about −120 to −60 km s^{-1}) and should be considered as a more reliable indicator of the velocity of the interstellar matter in these sightlines. The resulting velocities from Gaussian fits to the H I emission profiles are shown for comparison with the M31 DIBs in Field 3 in Figures 5–11.

CO peak velocities from radio observations by Nieten et al. (2006) are consistent with those of the H I gas. For Field 3, CO matches better with H I than Na I, which provides further evidence that our measured M31 Na I velocities for 4408.04, 4412.17, and 4417.80 are probably in error.

3.7. M31 H II Regions

In addition to the stars in Table 1, three H II regions were observed serendipitously in Field 3, spatially coincident with the GMOS slits of the stars 4408.79, 4408.94, and 4417.12. Using the relative strengths of the emission lines in these spectra, it is possible to derive an estimate for the interstellar metallicity in the vicinity of Field 3. The usefulness of these spectra is limited because they are not flux calibrated and the blue and red wavelength regions were recorded in separate exposures. Nevertheless, an estimate of the O/H abundance ratio can be obtained from the relative N II 6583 Å and Hα line fluxes (see Pettini & Pagel 2004).

The emission spectra were extracted from regions at the edges of the GMOS slits where the stellar flux was negligible, sky-subtracted using sky spectra from nearby slits showing no nebular emission, and continuum-subtracted using low-order polynomial fits. The final spectra are shown in Figure 15. The logarithmic flux ratios ($\log([N\,II]/H\alpha)$) for 4408.79, 4408.94, and 4417.12 are −0.54, −0.63, and −0.61, respectively, which correspond to oxygen abundances $12 + \log[O/H] = 8.59$, 8.53, and 8.51 (all with 1σ errors of ± 0.18), using Equation (2) of Pettini & Pagel (2004). The average value, 8.54 ± 0.18, is similar to that in the solar neighborhood, where the oxygen abundance of H II regions is in the range 8.45–8.50 (see Pilyugin et al. 2003 and references therein).

Our derived [O/H] ratios add to the limited data already available in the literature on the metallicity of M31. Trundle et al. (2002) reviewed the previous work on oxygen abundance measurements of H II regions in M31 and identified that there is some uncertainty in the metallicity gradient across M31. Measured oxygen abundance gradients range from −0.013 to −0.027 dex kpc^{-1}, depending on the method used to derive [O/H]. Extrapolating these gradients gives $12 + \log[O/H] =$ 8.70–9.21 at the center of M31, compared with 8.90 in the center of the MW. The three H II regions we observed are

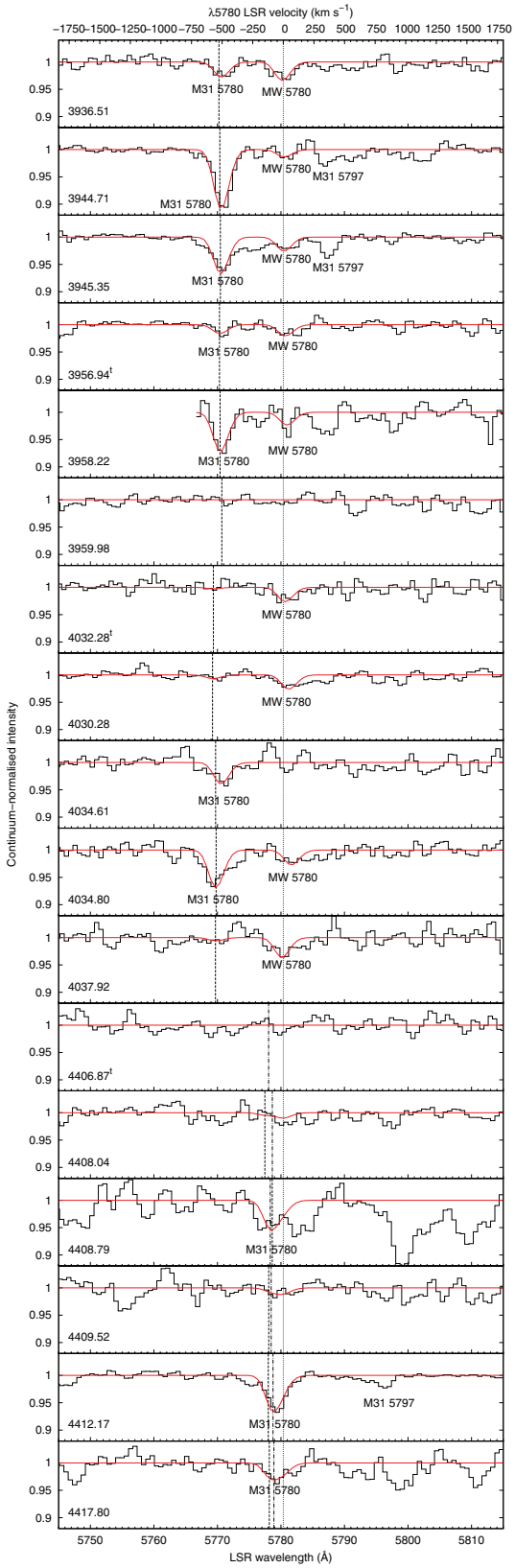

Figure 5. Observed continuum-normalized spectra of the λ5780 region (histograms). λ5780 components arising in MW and M31 have been fitted using the Galactic sightline β^1 Sco as a template (fitted profiles overlaid in red). Velocity scale at the top is relative to the Galactic λ5780 rest wavelength of 5780.37 Å (Galazutdinov et al. 2000; plotted with a vertical dotted line). The mean M31 interstellar Na I absorption wavelengths are plotted with vertical dashed lines. For the Field 3 stars, the peak H I velocities are also shown (dot-dashed lines). The superscript "t" denotes telluric standard stars.

(A color version of this figure is available in the online journal.)

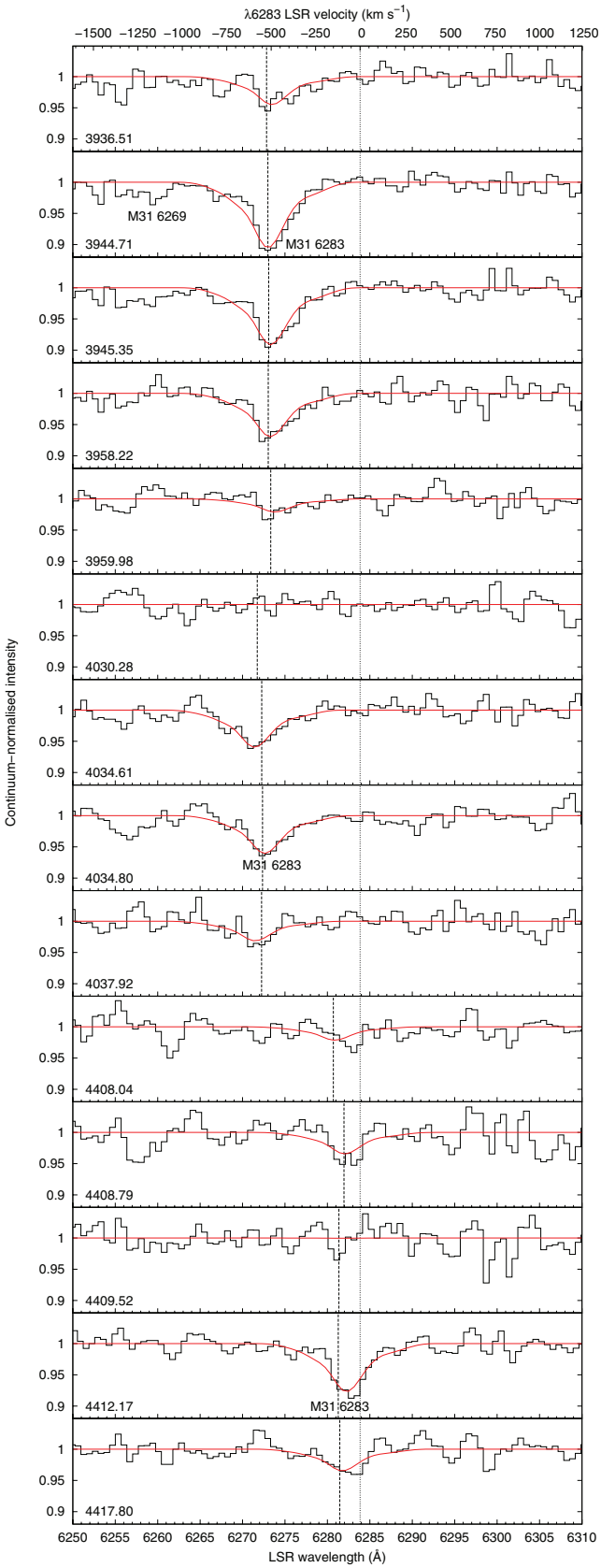

Figure 6. Observed continuum-normalized, telluric-corrected spectra of the λ6283 region (histograms), with fitted DIB profiles overlaid (red curves). Velocity scale at the top is relative to the Galactic λ6283 rest wavelength of 6283.85 Å (Galazutdinov et al. 2000; plotted with a vertical dotted line). The mean M31 interstellar Na I absorption wavelengths are plotted with vertical dashed lines.

(A color version of this figure is available in the online journal.)

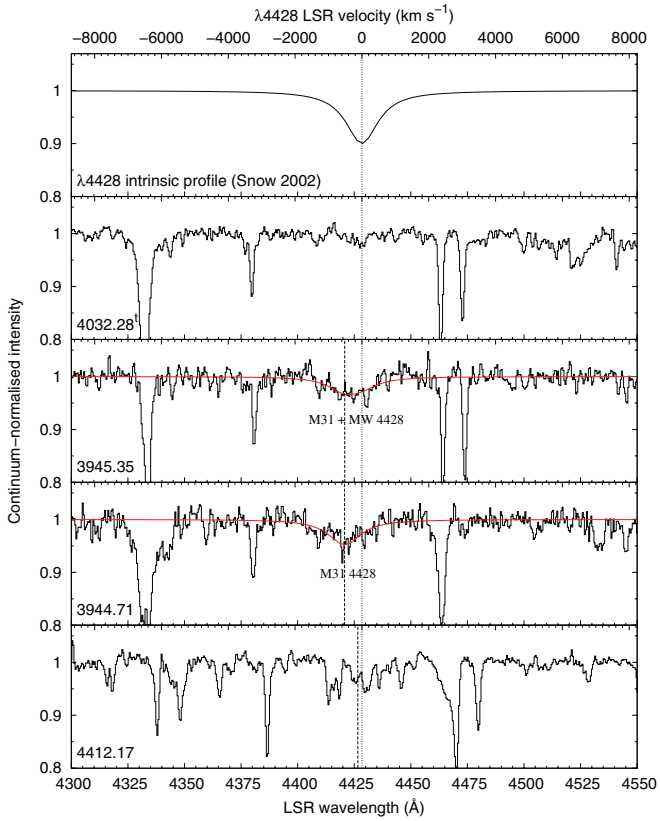

Figure 7. Observed continuum-normalized spectra of the λ4428 region (histograms). The upper panel shows the intrinsic MW λ4428 profile (Snow 2002a). Velocity scale at the top is relative to the Galactic DIB rest wavelength of 4428.39 Å (dotted line). M31 Na I velocities are plotted with dashed lines.

(A color version of this figure is available in the online journal.)

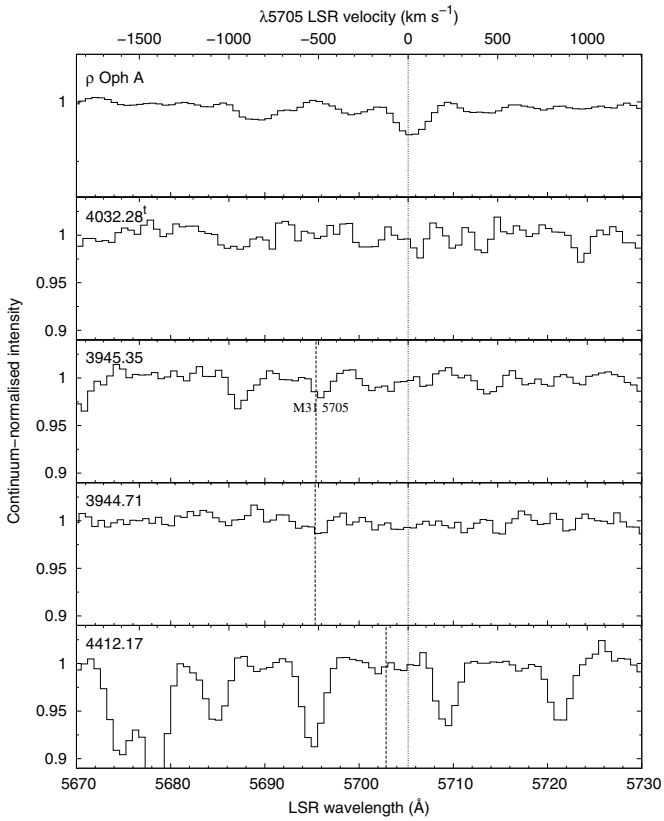

Figure 8. Observed continuum-normalized spectra of the λ5705 region. The upper panel shows MW comparison DIB spectrum toward ρ Oph A (Cordiner 2006). The second panel from the top shows the spectrum of one of the telluric standard stars. Velocity scales at the top of this figure and Figures 9–13 are relative to the Galactic DIB rest wavelengths published by Galazutdinov et al. (2000). The mean M31 interstellar Na I absorption wavelengths are plotted with vertical dashed lines. The spectrum of 4412.17 is dominated by stellar features at this wavelength.

approximately 23′ from the center of M31, which corresponds to 5.2 kpc (assuming a distance of 783 kpc to M31; Holland 1998). The average oxygen abundance in the three H II regions (8.54) lies toward the lower end of the range of values previously reported at this radius in M31.

Fields 1 and 2 lie at radial distances (r) of 63′ (14.3 kpc) and 41′ (9.3 kpc), respectively, from the center of M31. Using the metallicity relation of $12 + \log[\mathrm{O/H}] = 8.7–0.013r$, which was deduced from the study of B star abundances by Trundle et al. (2002), we find oxygen abundances of 8.51 and 8.58 for these two fields. Thus, there is no evidence to suggest that the metallicity of the ISM along any of our surveyed sightlines is significantly different from solar.

3.8. Interstellar Radiation Field

Near-ultraviolet interstellar radiation field strengths (NUV ISRFs) were calculated for the M31 ISM in each sightline, using the NUV *GALEX* mosaic of M31 (imaged at a central wavelength of 2271 Å) from Thilker et al. (2005). The NUV ISRF strengths (I_{NUV}) are given in Table 4 in units of the Galactic NUV ISRF of Draine (1978), integrated over the aperture size and NUV wavelength response function of the *GALEX* telescope. Maps of I_{NUV} for each of our three fields were computed from the *GALEX* image and are shown in Figure 17.

To calculate these I_{NUV} maps, individual pixel fluxes were background-subtracted and corrected for foreground extinction using $A_{\mathrm{NUV}} = 8.0 \times E_{B-V}$ (Gil de Paz et al. 2007), assuming an MW foreground extinction of 0.06 mag (see Section 3.4). The M31 extinction was derived for each field from the average of the E_{B-V}^{M31} values of the stars listed in Table 1. For each sightline in the ISRF maps, I_{NUV} was calculated at a point at a line-of-sight distance r halfway into the foreground M31 cloud, using the extinction–distance relation derived by Vergely et al. (1998) for the solar neighborhood ($dA_V/dr = 1.2$ mag kpc^{-1}, with $R_V = A_V/E_{B-V} = 3.1$), and assuming that the observed NUV flux is emitted from the image plane (at a radial distance of 783 kpc). The NUV photons were assumed to be subject to the same level of extinction as a function of distance as in the solar neighborhood; consequently, the calculated I_{NUV} are dominated by the flux from OB stars in the immediate vicinity of the interstellar clouds of interest; stars at distances greater than 1 kpc make a negligible contribution to the total NUV flux at a given point in space. The NUV ISRF strengths thus calculated are only approximate because they take no account of the fact that the shape of the extinction law, and the extinction as a function of distance in M31, may be different from that observed in the MW. The M31 foreground extinction is treated as a uniform slab of material, so any small-scale inhomogeneities in the M31 ISM are neglected.

Within Fields 1–3, respectively, the interstellar UV field strengths (I_{NUV}) averaged over all pixels are 0.24, 0.77, and 0.34 (in units of the Draine field), with an average value of 0.45. Evidently, even though these fields are relatively rich in OB stars, the NUV ISRF is still significantly weaker than that of the

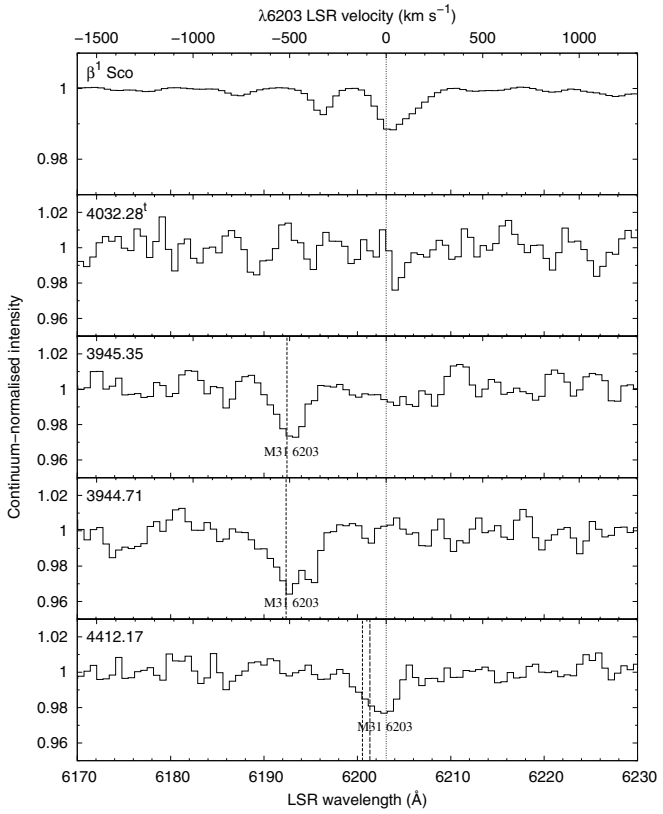

Figure 9. Observed continuum-normalized spectra of the λ6203 region. The upper panel shows MW comparison DIB spectrum toward β^1 Sco (Cordiner 2006). The DIB rest velocity is shown with a dotted line and the M31 Na I velocities are plotted with dashed lines. For 4412.17, the mean H I velocity is shown with a dot-dashed line.

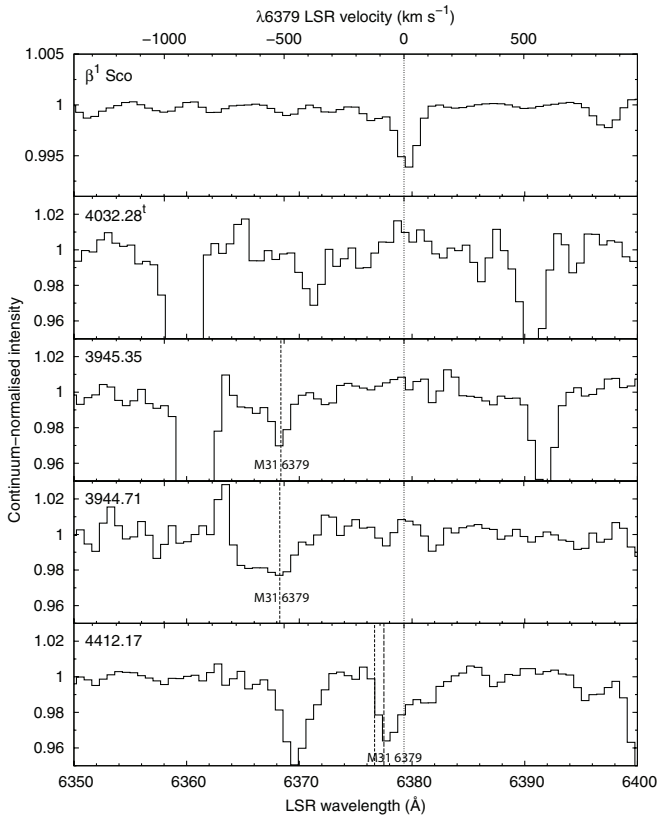

Figure 10. Observed continuum-normalized spectra of the λ6379 region. The upper panel shows MW comparison DIB spectrum toward β^1 Sco (Cordiner 2006). The DIB rest velocity is shown (dotted line), and the M31 Na I velocities are plotted with dashed lines. For 4412.17, the mean H I velocity is shown with a dot-dashed line. The strong absorption features around 6360 and 6390 Å are due to stellar S II and Ne I.

MW. This is consistent with the conclusions of previous authors (see Section 1). Field 2 has the greatest $I_{\rm NUV}$ values due to the presence of OB78 (NGC 206)—the richest OB association in M31. Indeed, the sightlines toward the DIB target stars in this field have NUV field strengths which are comparable to or greater than the (Draine 1978) Galactic value. On the other hand, most of the stars in Field 1 toward which DIBs are observed have $I_{\rm NUV} < 0.5$, including the star in our sample 3944.71, toward which the M31 DIBs are strongest.

3.9. Aromatics and Dust Emission

For the three M31 fields presented here, we obtained reduced infrared *Spitzer Space Telescope* images in the IRAC 8 μm and MIPS 24 μm bands from the surveys of Barmby et al. (2006) and Gordon et al. (2006). The flux in the 8 μm band is dominated by PAH emission from the 7.7 μm (and 8.6 μm) aromatic bands (see, for example, Draine & Li 2001 and Flagey et al. 2006), whereas the flux in the 24 μm band predominantly arises from interstellar dust. The ratio of 8 μm to 24 μm fluxes may therefore be used as an approximate measure of the relative PAH emission intensity per unit dust mass (e.g., Flagey et al. 2006; Engelbracht et al. 2008; Gordon et al. 2008), and as such, provides an indication of the abundance and excitation level of PAHs in the ISM.

The 8 μm IRAC images are shown for our three fields in Figure 17. The interstellar emission flux was measured for each of the sightlines in Table 4 from the background-subtracted *Spitzer* images using a ring median filter of radius 5 pixels and width 2 pixels in order to exclude the flux from stellar point sources. To measure the 8/24 μm interstellar flux ratio, the 8 μm images were convolved and rebinned to the lower spatial resolution of the 24 μm images using the convolution kernel provided by Gordon et al. (2008).

In the plane of the MW, the interstellar 8/24 μm flux ratio (R) varies between about 0.1 and 2.0, with a mean value of 1.6 (Flagey 2007). Similarly, in nearby spiral galaxies, R also varies between about 0.1 and 2, with considerable scatter within individual galaxies (Bendo et al. 2008). The ratio R correlates with metallicity, which has been interpreted as being due to variation in the strength of PAH emission relative to the 24 μm dust emission, at least partly as a result of differences in PAH abundances (Engelbracht et al. 2005). However, PAH emission correlates better with ionization of the ISM than the metallicity (Gordon et al. 2008; Bendo et al. 2008), so the 8 μm flux may be a better indicator of the degree to which the PAHs are ionized rather than their overall abundance. R also tends to be lower inside H II regions and higher in denser, dustier gas associated with photodissociation region boundaries.

In our GMOS fields, R values range between 0.63 and 1.78, with mean values of 1.05, 1.16, and 1.04 in Fields 1–3, respectively. Thus, there is nothing particularly unusual about the PAH emission in these fields compared with other galaxies, although the mean values are somewhat lower than observed in the MW. This is perhaps indicative of a reduced level of ionization or processing of the aromatic material in our M31 fields as a result of the lower UV radiation fields that are typical of M31.

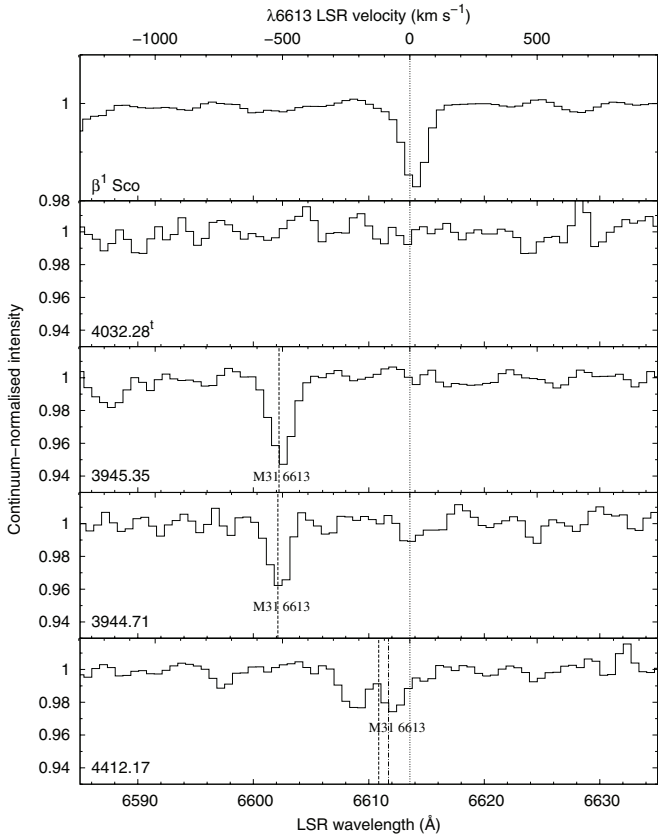

Figure 11. Observed continuum-normalized spectra of the λ6613 region. The upper panel shows MW comparison DIB spectrum toward β^1 Sco (Cordiner 2006). The DIB rest velocity is plotted (dotted line), and the M31 Na I velocities are plotted with dashed lines. For 4412.17, the mean H I velocity is shown with a dot-dashed line.

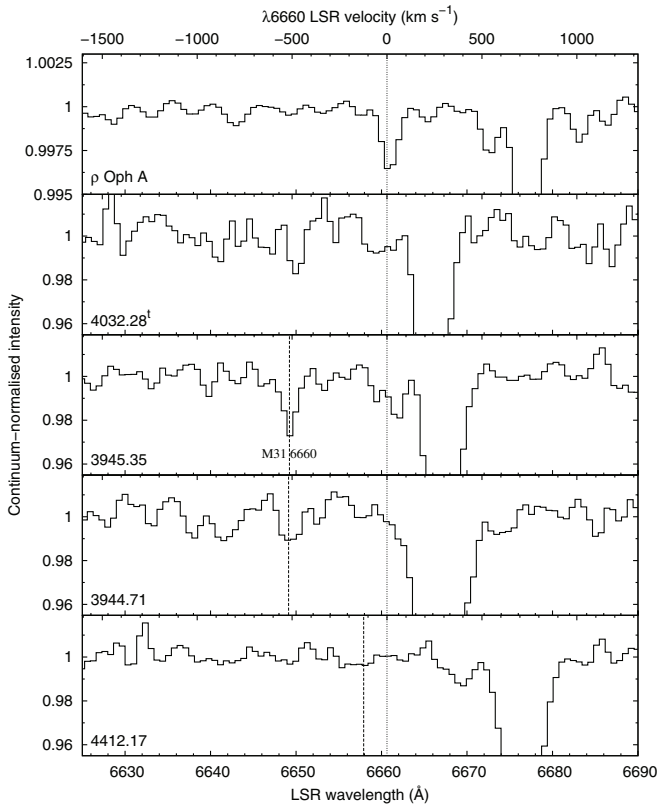

Figure 12. Observed continuum-normalized spectra of the λ6660 region (histograms). The upper panel shows MW comparison DIB spectrum toward ρ Oph A (Cordiner 2006). The DIB rest velocity and M31 Na I velocities are plotted with dotted lines. The strong stellar line at the red end is due to He I.

The strength of the 8 μm emission discussed here is at variance with previous studies (Cesarsky et al. 1998; Pagani et al. 1999) that identified anomalously weak aromatic mid-IR emission bands in the bulge and nucleus of M31. Thus, the PAH emission traced by the 8 μm flux, at least in our observed fields (which are away from the nucleus/bulge), is apparently not as weak as previously thought and implies that the PAHs in M31 may in fact not be dissimilar to those found in the MW and other spiral galaxies. It must be noted, however, that the NUV ISRF in our observed fields may be greater than is typical for M31 due to the concentration of OB stars, which could give rise to increased 8 μm emission in these regions relative to the average conditions in M31.

4. DIB STRENGTHS AND CORRELATIONS

Figure 16 shows the relationships between the equivalent widths of a selection of the strongest DIBs (λλ4428, 5780, 6283, 6379, 6613, and 6660) and interstellar reddening ($E^{\rm M31}_{B-V}$), for sightlines in M31 and the MW. All of the newly observed M31 DIB measurements lie within the range of values previously observed in the MW, apart from λ6660, which seems anomalously strong, perhaps due to spectral contamination, which may be indicated by reference to the telluric standard spectrum in Figure 12.

The majority of the M31 data points plotted in Figure 16 lie within the middle-to-upper part of the range of values covered by the MW data. Thus, per unit E_{B-V}, the M31 DIBs are as strong or stronger than those typically observed in the MW. The

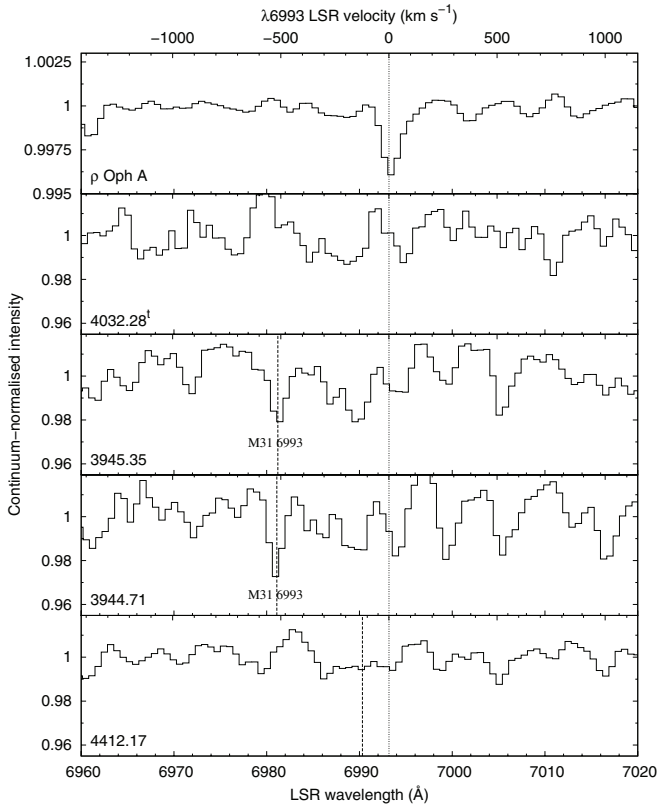

Figure 13. Observed continuum-normalized spectra of the λ6993 region. The upper panel shows MW comparison DIB spectrum toward ρ Oph A (Cordiner 2006). The DIB rest velocity and M31 Na I velocities are plotted with dotted lines.

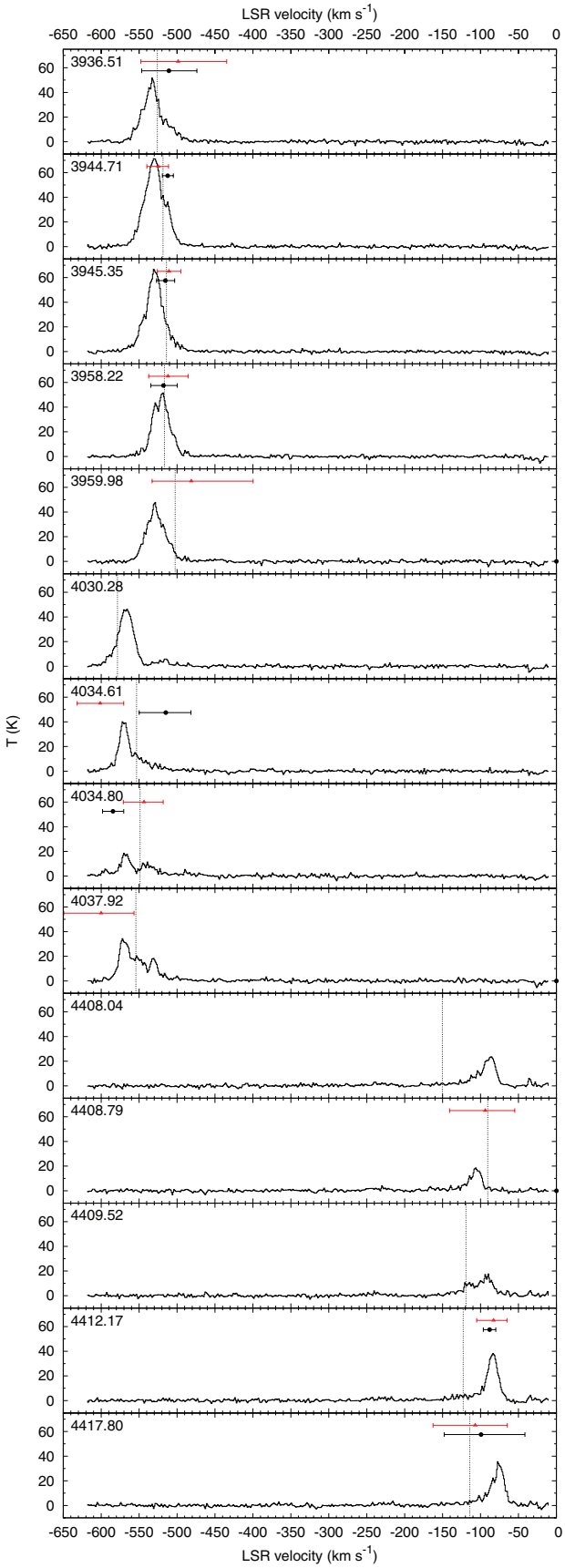

Figure 14. H I emission spectra derived from the survey by Braun et al. (2009). M31 Na I velocities are plotted with dotted vertical lines. λλ5780 and 6283 DIB velocities (and 1σ error bars) are plotted with black circles and red triangles, respectively.

(A color version of this figure is available in the online journal.)

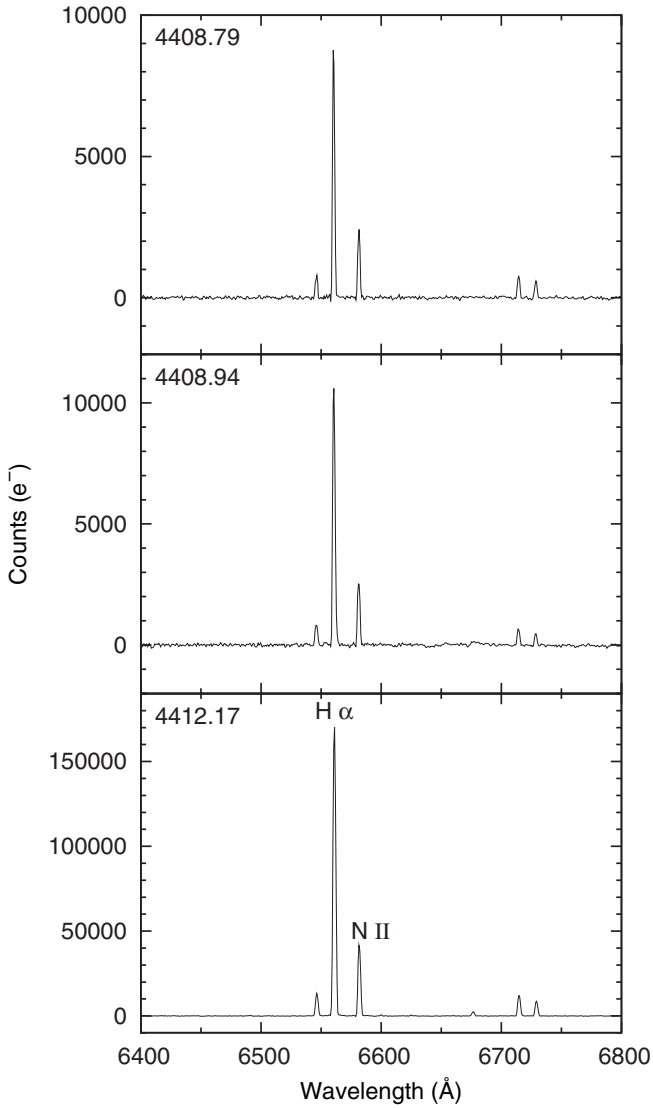

Figure 15. Sky-subtracted spectra from observed H II emission regions in the telluric rest frame. The N II 6583 Å and H α lines used to derive oxygen abundances are marked.

relative enhancement of DIB strengths is most pronounced for Field 1 (shown as black filled circles in the plots), for which the equivalent widths of the strongest (and therefore most reliably measured) DIBs λλ5780, 6283, and 6613 are clearly at the upper end of the range of Galactic values. The locations of those sightlines with the strongest DIBs are shown in Figure 17; the sizes of the circles indicate the relative strength of the λ6283 DIB per unit E_{B-V} in each sightline. It is evident that the ISM in Field 1 hosts the strongest DIBs per unit E_{B-V} and Fields 2 and 3 the weakest. The DIBs with the largest equivalent widths in our sample are toward 3944.71, 3945.35 in Field 1. These are the sightlines with the most reddening and the greatest H I column densities. Relative to the amount of dust in the 3944.71 sightline, the λλ5780, 6283, and 6613 equivalent widths are at the very upper limit of what has previously been observed in the MW, so these sightlines have exceptionally strong DIBs. As can be seen in Table 5, the majority of the measured DIBs in the sightlines toward 3944.71 and 3945.35 are significantly stronger than those in the MW, for the same reddening. These two sightlines have relatively low NUV ISRF strengths—about 0.5 and 0.4 times that of the MW, respectively.

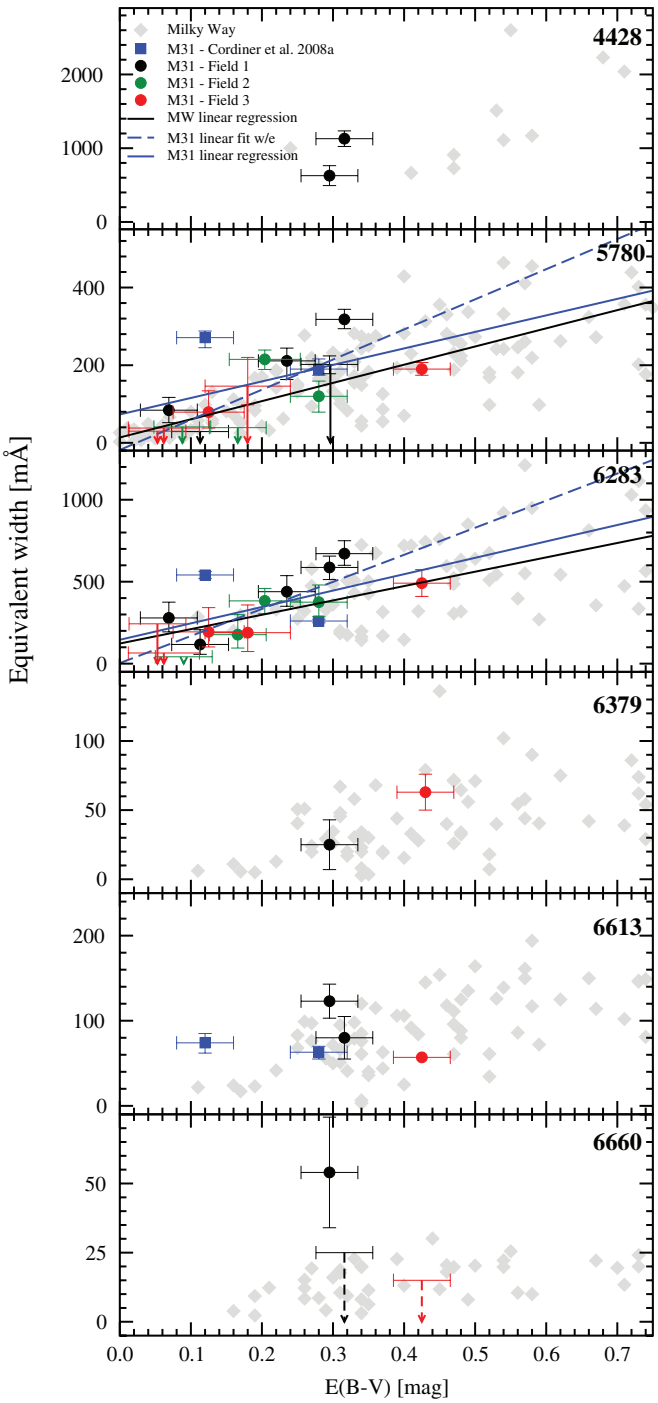

Figure 16. λλ4428, 5780, 6283, 6379, 6613, and 6660 DIB equivalent widths as a function of E_{B-V} for M31 and the MW. Data points for the three GMOS fields are plotted in different colors. Measurements from Cordiner et al. (2008a) are included (blue squares). DIB equivalent width upper limits are shown with downward-pointing arrows. MW DIB data are from Herbig (1993), Thorburn et al. (2003), Megier et al. (2005), and Cordiner (2006), and for λ4430, Herbig (1975). For the λλ5780 and 6283 DIBs, linear regressions are shown for the MW data (black solid lines) and the M31 data (blue solid lines). A linear fit that takes into account the errors in both ordinates is also shown for the M31 λλ5780 and 6283 data (dashed blue lines).

(A color version of this figure is available in the online journal.)

As derived in Section 3.4, the mean λ5780 equivalent width per unit reddening measured in the MW is $[W(5780)/E_{B-V}]_{\rm mean} = 0.53 \pm 0.23$ Å mag^{-1}. Using data on the λ6283 DIB from the same Galactic literature,

Table 5
DIB Equivalent Widths for Targets with Many DIB Detections

Sightline	3944.71	3945.35	4412.17	MW ISM	⋆	⋆
Sp. Type	O9.7 Ib	B6 Ia	B2.5 Ia	Avg.	B0 Ia	B9 Ia
E_{B-V}	0.32	0.33	0.43	0.32	0	0
W(4428)	1129 (106)	628 (135)	[a]	865	640	370
W(5705)	<31	42 (25)	<19	38	5	8
W(5780)	318 (25)	202 (23)[a]	190 (17)	163	2	30
W(5797)	62 (35)	101 (28)	45 (21)	49	4	9
W(6203)	159 (65)	93 (54)	92 (40)	54	5	4
W(6269)	60 (23)	[a]	<14	...	0	7
W(6283)	671 (75)	587 (73)	491 (82)	362	1	10
W(6379)	[a]	25 (18)	63 (13)[a]	28	8	1
W(6613)	80 (25)	123 (20)	57 (15)	68	0	5
W(6660)	<25	54 (20)	<15	16	0	1
W(6993)	45 (23)	77 (19)	<14	38	0	2

Notes. DIB equivalent widths are in mÅ. Average DIB strengths (per unit E_{B-V}) for the Galactic diffuse ISM (scaled to $E_{B-V} = 0.32$) are given in the column labeled MW ISM (data from Herbig 1993, Thorburn et al. 2003, Megier et al. 2005, and Cordiner 2006). No large sample of λ6269 measurements is available. Possible stellar line contributions (in mÅ) to DIB equivalent widths are given in the columns labeled ⋆ for B0 Ia and B9 Ia stars, measured from synthetic stellar spectra with temperatures of 28,000 and 10,000 K, respectively.

[a] Uncertain (or unmeasurable) equivalent widths due to line blends.

$[W(6283)/E_{B-V}]_{\rm mean} = 1.18 \pm 0.53$ Å mag^{-1}. The errors are the standard deviations of the respective data. The mean values for $W(5780)/E_{B-V}$ in Fields 1, 2, and 3 are 0.93, 0.7, and 0.73 Å mag^{-1}, respectively, and for $W(6283)/E_{B-V}$, 2.4, 1.37, and 1.27. These values are consistent with the identified trend that our observed M31 DIBs are relatively strong compared with the MW and highlight, in particular, the strengths of these DIBs in Field 1.

The weakest DIBs (per unit E_{B-V}) are observed toward 4030.28, 4034.61, and 4037.92 in Field 2 and 4412.17 in Field 3. These four sightlines are near regions of strong UV flux (see Figure 17) and include the strongest NUV ISRFs of the observed sightlines, with $I_{\rm NUV} \gtrsim 1$. The smallest $W(6283)/E_{B-V}$ value is observed toward 4030.28, where $I_{\rm NUV}$ is largest, and the largest $W(6283)/E_{B-V}$ value is observed toward 3936.51, where $I_{\rm NUV}$ is smallest, which is suggestive of a correlation between the interstellar UV field and DIB strengths. To analyze this correlation, the equivalent widths per unit reddening of the two strongest DIBs (with the smallest relative measurement errors), λλ5780 and 6283, are plotted with respect to the NUV ISRF strength in Figure 18. There is a significant negative correlation between $W/E_{B-V}^{\rm M31}$ and $I_{\rm NUV}$ for both DIBs at the 68% confidence level, shown by the gray polygon. The correlation coefficients between the data for λλ5780 and 6283 are −0.55 and −0.41, respectively. This indicates that as the interstellar UV flux increases, the abundances of both of these DIB carriers tend to become less, relative to the amount of dust. Plausible explanations for this phenomenon are that the DIB carriers become ionized or are photodissociated, or that the chemical environments in which the carriers form are destroyed by NUV radiation.

A link between UV flux and DIB strengths is corroborated by the pattern of DIB observations in Field 2 and the morphology of the ISM in this region. This field covers the OB78 association, which is the largest, most active region of recent star formation in M31. Most of the stars at the heart of this association do not show significant reddening or DIBs (see Figure 17)—the majority of the gas and dust around these stars has been blown

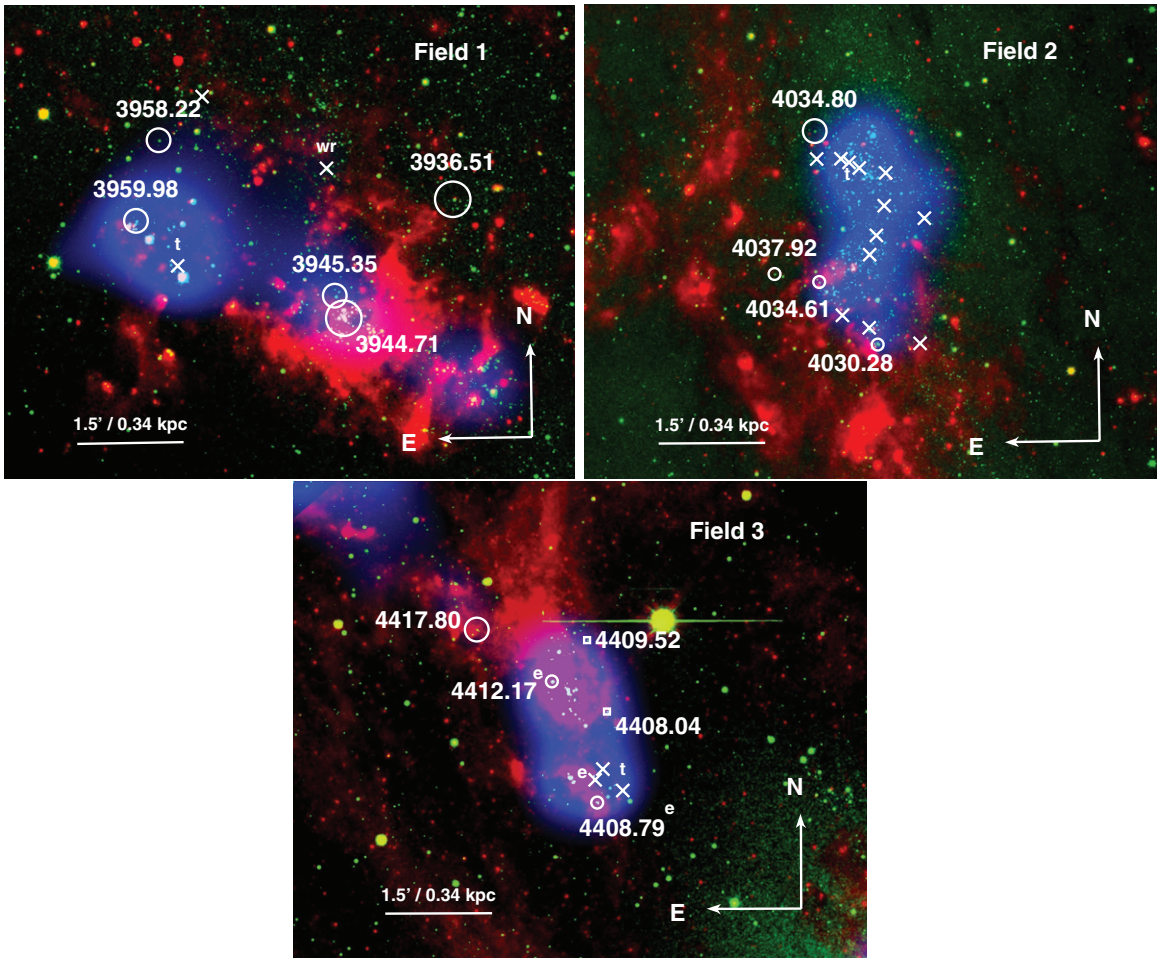

Figure 17. Three-color composite maps of our observed M31 fields. Blue corresponds to the NUV ISRF (see Section 3.8), green is the optical *V*-band image (Massey et al. 2006), and red is the *Spitzer* IRAC 8 μm data that trace PAH emission (Section 3.9). Intensities are shown on a logarithmic scale. ISRF values range from 0.05 to 0.5, 6.0, and 1.0 Draine for Fields 1–3, respectively. 8 μm flux values range from 0.0 to 50.0 MJy sr^{-1} for all fields. Lines of sight with M31 DIBs are marked with circles, the sizes of which denote the strength of the λ6283 DIB per unit reddening (relative to the mean M31 DIB strength): small, 10″ circles denote weak; medium, 20″ circles denote average; and large, 30″ circles denote strong DIBs. Crosses indicate sightlines with no DIB detections, squares denote upper limits. Also marked are the telluric standards (t), the H II emission regions (e), and the single Wolf–Rayet star observed in Field 1 (wr). The two targets with previously observed DIBs reported by Cordiner et al. (2008a) are about 6 arcmin (≈1.3 kpc) south of Field 2.

away by strong stellar winds and supernovae (Brinks & Shane 1984; Loinard et al. 1996), creating a large, hollow region in the ISM several hundred parsecs across. There is still sufficient interstellar matter at the periphery of the central cluster that DIBs are observed toward many of the nearby stars, and the 8 μm flux is intensely strong as a result of the high UV-optical flux that excites the interstellar aromatics. The DIBs are generally quite weak in this field compared to the M31 average, which we suggest is due to the destruction by strong UV irradiation of the environments in which the carriers form.

The relationship between DIB strengths and UV flux has been examined previously in the MW and in the MCs. Indeed, the relative weakness of the DIBs observed in the MCs may be attributable to the strong radiation fields that pervade these galaxies (Cox et al. 2006; Cordiner 2006; Welty et al. 2006). UV-rich regions such as those found in the vicinity of the Orion Nebula and Scorpius are also known to show weak DIBs (Cami et al. 1997; Snow et al. 1995). Welty et al. (2006) found no significant correlation between UV flux and DIB strengths in the MCs. However, the UV field strengths in their analysis were derived from H_2 excitation, and it is known that the DIB carriers do not predominantly reside in the relatively dense regions of the ISM traced by H_2 (e.g., Herbig 1993).

The narrow ($\lambda\lambda$5797, 6613, 6660, and 6993) DIBs are enhanced toward 3945.35 with respect to the average MW diffuse ISM, while the broad DIBs are not. On the other hand, the line of sight toward 3944.71 (where the DIBs are strongest) shows enhanced broad ($\lambda\lambda$5780, 6203, and 6283) DIBs with respect to the average MW value. Previous studies on the MW (e.g., Cami et al. 1997; Krelowski et al. 1998) identified that these broad DIBs tend to be strong in relatively strongly UV-irradiated sightlines (where the narrow DIBs are weak), whereas narrow DIBs are strong in well-shielded sightlines. However, the negative correlation we have identified between the strengths of the $\lambda\lambda$5780 and 6283 DIBs and I_{NUV} suggests that the environments or the carriers of these DIBs are destroyed by UV radiation. Their large strengths in relatively strongly irradiated Galactic sightlines seem to be at odds with our observed correlation, but could instead be evidence for the production of enhanced quantities of DIB carriers as a result of photochemistry or dust photoabrasion in these Galactic regions. Indeed, it is notable from Figure 17 that the two sightlines with the strongest DIBs (3944.71 and 3945.35) reside in a region of both strong 8 μm flux (indicative of dense, dusty gas) and moderately high UV field strength. Given the association of mid-IR emission with ionized PAHs (Tielens 2008), this suggests that

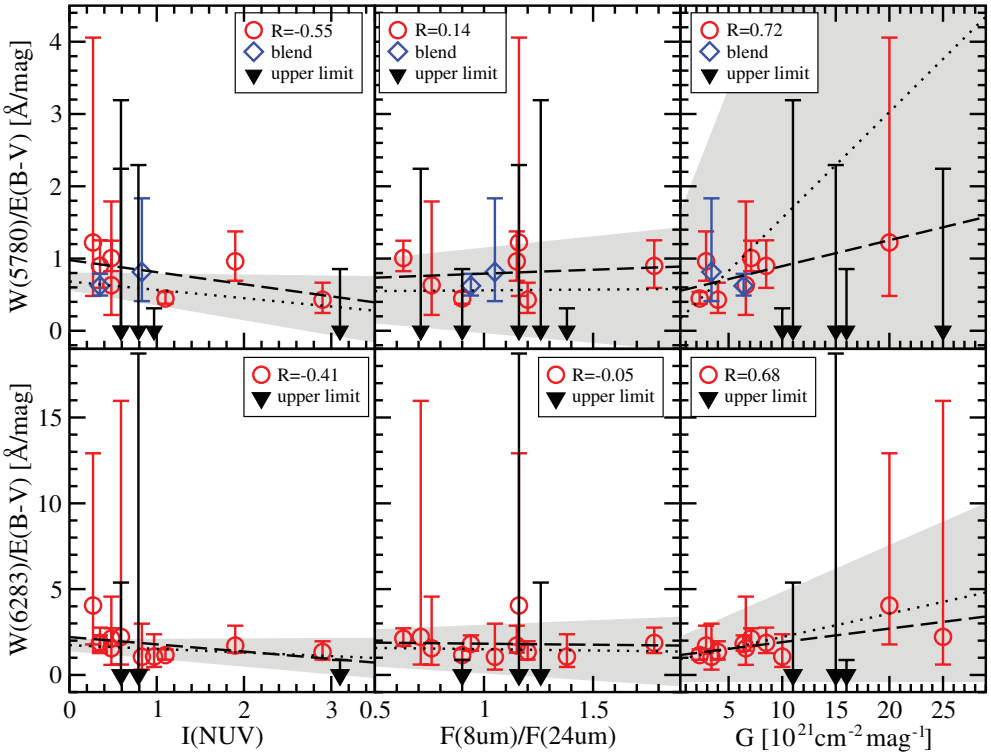

Figure 18. Correlations between λλ5780 and 6283 DIB equivalent widths per unit E_{B-V} and interstellar physical/chemical properties: interstellar UV field strength ($I_{\rm NUV}$), *Spitzer* 8/24 μm flux, and logarithmic gas-to-dust ratio (G). Linear regressions have been plotted (dashed lines) and correlation coefficients R are displayed on the top right. Fits that take into account the error bars are shown with dotted lines, the 1σ ranges for which are shown with gray polygons. Fitting excludes blended DIBs and upper limits.

(A color version of this figure is available in the online journal.)

Table 6
Fit Parameters for M31 λλ5780 and 6283 DIB Equivalent Widths Versus Reddening

DIB	Intercept a	Slope b	Correlation Coefficient R
MW 5780	14 ± 10	469 ± 29	0.81
M31 5780	73 ± 62	426 ± 234	0.60
MW 6283	123 ± 80	876 ± 174	0.55
M31 6283	146 ± 102	1000 ± 430	0.57

Notes. Equivalent width $W = a + (b \times E_{B-V})$. The outlier data from MAG 70817 (Cordiner et al. 2008a) were omitted from the fits.

the carriers of the λλ5780, 6203, and 6283 diffuse bands may be ionized molecules.

The correlations between λλ5780 and 6283 and E_{B-V} are shown in Figure 16. Taking into account the error bars on W and E_{B-V}, least-squares linear fits to the data result in the parameters shown in Table 6. Within the quoted 1σ errors, there are no significant differences between the slopes and intercepts of M31 and MW data for either DIB. Kolmogorov–Smirnov (K-S) tests were applied to the residuals of the observed data compared with the MW fits. The resulting probabilities $(1 - P)$ describe the likelihood that the M31 and MW DIB data have different distributions with respect to E_{B-V}. For λ5780, $(1 - P) = 0.93$, which shows there is a high statistical probability that the M31 and MW DIBs follow a different relationship with E_{B-V}. This is consistent with our observation that the M31 DIBs are typically rather strong compared with those in the MW. For λ6283, the derived value of $(1 - P) = 0.50$ is inconclusive and indicates that more observational data are needed.

Relatively weak DIBs are observed toward 4412.17 which has a very low G value; relatively strong DIBs are observed toward 3936.51, which has a high G value. These results could be explained if variations in G are caused by the destruction of dust grains (by shocks and UV radiation), and if the grain degradation products contain or give rise to the DIB carriers. Conversely, if gas-phase species are depleted out onto the dust, reducing the gas-to-dust ratio, then molecular DIB carriers would also accrete onto the grains, making the bands weaker. However, when accounting for the substantial errors in G across all sightlines, there is no statistically significant correlation between the gas-to-dust ratio and $W(5780)$ or $W(6283)$, as shown by the gray polygons in Figure 18. We know of no prior reports of correlations between DIB strengths and G in the MW; in the LMC, W/E_{B-V} and G have been shown to be uncorrelated, albeit with a very limited number of data points (Cox et al. 2006; Cordiner 2006). Thus, an alternative explanation may be required for the weakness of the DIBs toward 4412.17, perhaps related to the relatively high strength of the 8 μm emission at the position of this star. This indicates the presence of dense, dusty gas of the kind where DIBs tend to be relatively weak in the MW (Snow et al. 1995).

In Section 3.9, the relationship between the mid-IR 8/24 μm *Spitzer* flux ratios and the abundance of PAHs was discussed. Given that some of the DIBs are hypothesized to be caused by electronic transitions of neutral and ionized PAHs (the same classes of molecules believed to cause the 8 μm emission), it is of interest to look for a correlation between the DIB strengths and the mid-IR flux ratio. However, as shown in Figure 18, there is no relation evident between the strengths of λλ5780 and 6283 per unit E_{B-V} and the 8/24 μm ratios observed in our M31 sightlines. This indicates that the carriers of these particular DIBs are not the same as the aromatics which are predominantly

responsible for the 8 μm emission. There is some uncertainty in this result due to the fact that—in common with the H I 21 cm emission—it is impossible to separate the background contributions to the IR flux in our observed sightlines, so no definitive conclusions may be drawn. Nevertheless, it is apparent from the maps in Figure 17 that the distributions of sightlines with strong or weak DIBs do not generally follow the 8 μm emission intensity.

The exceptionally strong DIBs that were previously detected by Cordiner et al. (2008a) toward MAG 70817 in OB78 now seem to be unusual compared with typical M31 and MW trends. The strong λ5780 DIBs reported in the more extensive Keck DEIMOS study of OB78 by Cox & Cordiner (2008) were known to have large error bars on W and E_{B-V}, and the deduction of that study, that the M31 DIBs are substantially stronger than those observed in the MW, is not supported by the more accurate and statistically meaningful results presented here.

Past studies, highlighted in Section 1, have discovered different dust extinction and polarization properties in M31 compared to the MW, and in particular, a lack of small graphitic dust grains and an abundance of (relatively less UV-processed) PAHs. The similarity of the DIB spectrum to that in the MW indicates that the cause of these differences in the dust properties has little impact on the DIB carriers. That markedly different UV-extinction and optical polarization curves have been observed in M31 adds to the body of evidence that DIB carriers are not closely related to larger interstellar dust particles or to the smaller graphitic grains believed to be responsible for the 2175 Å UV extinction bump. However, studies of M31 dust and extinction have so far been very limited, and little is presently known about the detailed characteristics of the average M31 extinction curve. Further dedicated studies of this are warranted.

The general lack of UV/FUV radiation throughout M31 compared with the MW (see Section 1), due to the relatively low numbers of young stars, apparently does not have a detrimental effect on the DIB carrier abundances. Thus, it seems that the processing of interstellar material by strong, hard UV radiation may not be required to produce DIB carriers. There is still, however, a significant NUV flux throughout much of M31 (which, in the vicinity of dense clusters of OB stars, matches or exceeds the MW average), so the requirement for lower-energy UV photons in the production of DIB carriers cannot be ruled out.

5. CONCLUSION

We obtained optical spectra of over 30 early-type stars in three fields in M31 using the GMOS. Spectral classifications were presented, comprising the first spectral types for 20 of these stars. Reddenings (E_{B-V}) toward our targets were calculated, including the foreground-corrected M31 component. The M31 and MW components of interstellar Na I toward the most reddened subset of our targets were measured and their column densities, Doppler widths, and peak radial velocities derived.

Eleven DIBs (λλ4428, 5705, 5780, 5797, 6203, 6269, 6283, 6379, 6613, 6660, and 6993) have been detected in the M31 ISM, with profiles and patterns of strengths similar to those found in the MW and with radial velocities generally matching the interstellar Na I and H I and the stellar velocities. Measured radial velocities of the stars and interstellar matter match those of previously observed emission-line objects at the same projected galactocentric radii in M31.

The M31 λλ5780 and 6283 DIB equivalent widths as a function of E_{B-V} fall within the envelope of values typically seen in the MW. However, contrary to LMC and SMC DIBs which are weaker than those in the Galaxy, the M31 sightlines generally have DIBs that are as strong or slightly stronger than the average Galactic values. The M31 and MW DIB W versus E_{B-V} distributions were compared using a K-S test, which yielded a 93% probability that the observed M31 λ5780 DIB data are different from that of the MW. However, this statistic does not account for the errors in the data values. We measure a mean M31 λ5780 DIB equivalent width per unit reddening of $[W(5780)/E_{B-V}]_{\rm mean} = 0.78^{+0.72}_{-0.30}$, compared with 0.53 ± 0.23 Å mag^{-1} in the MW. Similarly, $[W(6283)/E_{B-V}]_{\rm mean} = 1.81^{+2.98}_{-0.81}$ Å mag^{-1}, compared with the MW value 1.18 ± 0.53 Å mag^{-1}. Thus, although the observed mean values are indicative of stronger-than-average DIBs within M31, the sizes of the error bars preclude the identification of any significant differences between the DIB strengths in M31 and the MW. Higher S/N observations of more M31 sightlines are required to resolve this issue.

A correlation between DIB strengths and $I_{\rm NUV}$ has been found at a 68% confidence level, which indicates that the DIB carrier abundances are enhanced in regions with weaker UV interstellar photon flux. We therefore hypothesize that the general lack of UV photons in parts of M31 benefits the survival of DIB carriers and their chemical precursors against photodestruction and that FUV radiation is not a requirement for the production of DIB carriers.

The DIBs observed in the spectrum of 3944.71 are very strong per unit E_{B-V}. It is clear, however, that the unusually strong DIBs previously detected in M31 by Cordiner et al. (2008a) and Cox & Cordiner (2008) are anomalous with respect to the average M31 trend, and that in general, the relationship between M31 DIB equivalent widths and reddening is very similar to that of the MW. The degree of scatter of the M31 DIBs around the average relationship (per unit E_{B-V}) is also similar to that observed in the Galaxy.

The similarity of the M31 DIB W/E_{B-V} relation to that of the MW suggests that DIB equivalent widths may be applicable as probes of E_{B-V} in other, similar spiral galaxies. However, there is evidence that the relationship for M31 is slightly different, perhaps as a result of the low UV field strength, and therefore further study of DIBs in external galaxies is warranted. Particular caution must be exercised when using DIBs as a measure of reddening in galaxies with substantially different metallicities, gas-to-dust ratios, and ISRF strengths (such as the MCs).

When taking into account the substantial errors on G, the strengths of the λλ5780 and 6283 DIBs (measured by W/E_{B-V}) do not show any significant correlation with the gas-to-dust ratio G.

No significant correlation is found between W/E_{B-V} and the 8/24 μm flux ratio for the λλ5780 and 6283 DIBs, indicating that the (PAH) carriers of the 8 μm infrared band are not closely related to these DIB carriers. The 8/24 μm and gas-to-dust ratios in our fields are in the range of values previously observed in the MW, so in these respects the gas and dust properties of M31 are not found to be distinguishably different from those of the Galaxy.

Finally, it should be noted that our results reflect the behavior of the ISM in only three small regions of M31 and therefore do not necessarily reflect the global behavior of the M31 disk. However, our regions do span a range of galactocentric distances and have a range of different properties in terms of the structure and composition of the gas, the density and type of stellar

objects, the radiation field strength and the metallicity, and are therefore indicative of the DIB behavior expected throughout much of the rest of the disk.

This paper is based on observations (GN-2007B-Q-116) obtained at the Gemini Observatory, which is operated by the Association of Universities for Research in Astronomy, Inc., under a cooperative agreement with the NSF on behalf of the Gemini partnership. For financial support, M.A.C. acknowledges the NASA Institute for Astrobiology, N.L.J.C. acknowledges the Faculty of the European Space Astronomy Centre (ESAC), and K.T.S. acknowledges the Engineering and Physical Sciences Research Council (EPSRC). M.A.C. and K.T.S. thank ESAC for visitor funding. We thank Dr. Fabio Bresolin for discussions regarding the H II region spectra and metallicities, Professor Paul Crowther for his classification of 3945.82, and Dr. Ian Hunter for his spectral synthesis calculations. We gratefully acknowledge Professor Elias Brinks and Dr. Robert Braun for providing their M31 21 cm data. This research has made use of the SIMBAD database (operated at CDS, Strasbourg, France), and SAOImage DS9 (developed by Smithsonian Astrophysical Observatory).

Facilities: Gemini:Gillett, Spitzer

REFERENCES

Bajaja, E., & Gergely, T. E. 1977, A&A, 61, 229
Barmby, P., et al. 2006, ApJ, 650, L45
Bendo, G. J., et al. 2008, MNRAS, 389, 629
Bianchi, L., Clayton, G. C., Bohlin, R. C., Hutchings, J. B., & Massey, P. 1996, ApJ, 471, 203
Bianchi, L., Lamers, H. J. G. L. M., Hutchings, J. B., Massey, P., Kudritzki, R., Herrero, A., & Lennon, D. J. 1994, A&A, 292, 213
Bohlin, R. C., Savage, B. D., & Drake, J. F. 1978, ApJ, 224, 132
Braun, R., Thilker, D. A., Walterbos, R. A. M., & Corbelli, E. 2009, ApJ, 695, 937
Bresolin, F., Kudritzki, R.-P., Lennon, D. J., Smartt, S. J., Herrero, A., Urbaneja, M. A., & Puls, J. 2002, ApJ, 580, 213
Brinks, E., & Shane, W. W. 1984, A&AS, 55, 179
Burstein, D., & Heiles, C. 1978, ApJ, 225, 40
Cami, J., Sonnentrucker, P., Ehrenfreund, P., & Foing, B. H. 1997, A&A, 326, 822
Cesarsky, D., Lequeux, J., Pagani, L., Ryter, C., Loinard, L., & Sauvage, M. 1998, A&A, 337, L35
Clayton, G. C., Wolff, M. J., Gordon, K. D., Smith, P. S., Nordsieck, K. H., & Babler, B. L. 2004, AJ, 127, 3382
Cordiner, M. A. 2006, PhD thesis, Univ. Nottingham, UK
Cordiner, M. A., Cox, N. L. J., Trundle, C., Evans, C. J., Hunter, I., Przybilla, N., Bresolin, F., & Salama, F. 2008a, A&A, 480, L13
Cordiner, M. A., Smith, K. T., Cox, N. L. J., Evans, C. J., Hunter, I., Przybilla, N., Bresolin, F., & Sarre, P. J. 2008b, A&A, 492, L5
Cox, N. L. J., & Cordiner, M. A. 2008, in IAU Symp. 251, Organic Matter in Space, ed. S. Kwok (Cambridge: Cambridge Univ. Press), 237
Cox, N. L. J., Cordiner, M. A., Cami, J., Foing, B. H., Sarre, P. J., Kaper, L., & Ehrenfreund, P. 2006, A&A, 447, 991
Cox, N. L. J., & Patat, F. 2008, A&A, 485, L9
Cox, N. L. J., et al. 2007, A&A, 470, 941
D'Odorico, S., di Serego Alighieri, S., Pettini, M., Magain, P., Nissen, P. E., & Panagia, N. 1989, A&A, 215, 21
Draine, B. T. 1978, ApJS, 36, 595
Draine, B. T. 2003, ApJ, 598, 1017
Draine, B. T., & Li, A. 2001, ApJ, 551, 807
Ehrenfreund, P., & Foing, B. H. 1996, A&A, 307, L25
Ehrenfreund, P., et al. 2002, ApJ, 576, L117
Ellison, S. L., York, B. A., Murphy, M. T., Zych, B. J., Smith, A. M., & Sarre, P. J. 2008, MNRAS, 383, L30
Engelbracht, C. W., Gordon, K. D., Rieke, G. H., Werner, M. W., Dale, D. A., & Latter, W. B. 2005, ApJ, 628, L29
Engelbracht, C. W., Rieke, G. H., Gordon, K. D., Smith, J., Werner, M. W., Moustakas, J., Willmer, C. N. A., & Vanzi, L. 2008, ApJ, 678, 804
Ferlet, R., Vidal-Madjar, A., & Gry, C. 1985, ApJ, 298, 838
Flagey, N. 2007, PhD thesis,Université Paris Sud, France
Flagey, N., Boulanger, F., Verstraete, L., Miville Deschenes, M. A., Noriega Crespo, A., & Reach, W. T. 2006, in ASP Conf. Ser. 357, The Spitzer Space Telescope: New Views of the Cosmos, ed. L. Armus & W. T. Reach (San Francisco, CA: ASP), 85
Galazutdinov, G. A., Moutou, C., Musaev, F. A., & Krelowski, J. 2002, A&A, 384, 215
Galazutdinov, G. A., Musaev, F. A., Krełowski, J., & Walker, G. A. H. 2000, PASP, 112, 648
Gil de Paz, A., et al. 2007, ApJS, 173, 185
Gordon, K. D., Engelbracht, C. W., Rieke, G. H., Misselt, K. A., Smith, J., & Kennicutt, R. C., Jr. 2008, ApJ, 682, 336
Gordon, K. D., et al. 2006, ApJ, 638, L87
Hartmann, D., & Burton, W. B. 1997, in Atlas of Galactic Neutral Hydrogen, ed. D. Hartmann & W. B. Burton (Cambridge: Cambridge Univ. Press), 243
Herbig, G. H. 1975, ApJ, 196, 129
Herbig, G. H. 1993, ApJ, 407, 142
Herbig, G. H. 1995, ARA&A, 33, 19
Hobbs, L. M. 1974, ApJ, 191, 381
Hobbs, L. M., et al. 2008, ApJ, 680, 1256
Hobbs, L. M., et al. 2009, ApJ, 705, 32
Holland, S. 1998, AJ, 115, 1916
Howarth, I. D., Price, R. J., Crawford, I. A., & Hawkins, I. 2002, MNRAS, 335, 267
Hubeny, I., & Lanz, T. 2000, in SYNSPEC–A User's Guide, http://nova.astro.umd.edu/Tlusty2002/pdf/syn43guide.pdf
Humphreys, R. M., Massey, P., & Freedman, W. L. 1990, AJ, 99, 84
Hutchings, J. B., Bianchi, L., Lamers, H. J. G. L. M., Massey, P., & Morris, S. C. 1992, ApJ, 400, L35
Johnson, H. L. 1966, ARA&A, 4, 193
Kalberla, P. M. W., Burton, W. B., Hartmann, D., Arnal, E. M., Bajaja, E., Morras, R., & Pöppel, W. G. L. 2005, A&A, 440, 775
Kang, Y., Bianchi, L., & Rey, S. 2009, ApJ, 703, 614
Kendall, T. R., Mauron, N., McCombie, J., & Sarre, P. J. 2002, A&A, 387, 624
Krelowski, J., Galazutdinov, G. A., & Musaev, F. A. 1998, ApJ, 493, 217
Kumar, C. K. 1979, ApJ, 230, 386
Kurucz, R. 1993, ATLAS9 Stellar Atmosphere Programs and 2 km s^{-1} Grid, Kurucz CD-ROM No. 13 (Cambridge, MA: Smithsonian Astrophysical Observatory)
Lawton, B., Churchill, C. W., York, B. A., Ellison, S. L., Snow, T. P., Johnson, R. A., Ryan, S. G., & Benn, C. R. 2008, AJ, 136, 994
Lennon, D. J., Dufton, P. L., & Fitzsimmons, A. 1992, A&AS, 94, 569
Lequeux, J. 2000, in Proc. 232, WE-Heraeus Seminar, ed. E. M. Berkhuijsen, R. Beck, & R. A. M. Walterbos (Aachen: Shaker Verlag), 63
Loinard, L., Dame, T. M., Koper, E., Lequeux, J., Thaddeus, P., & Young, J. S. 1996, ApJ, 469, L101
Massey, P., Armandroff, T. E., & Conti, P. S. 1986, AJ, 92, 1303
Massey, P., Armandroff, T. E., Pyke, R., Patel, K., & Wilson, C. D. 1995, AJ, 110, 2715
Massey, P., Olsen, K. A. G., Hodge, P. W., Strong, S. B., Jacoby, G. H., Schlingman, W., & Smith, R. C. 2006, AJ, 131, 2478
McCall, B. J., et al. 2010, ApJ, 708, 1628
Megier, A., Aiello, S., Barsella, B., Casu, S., & Krełowski, J. 2001, MNRAS, 326, 1095
Megier, A., Krełowski, J., & Weselak, T. 2005, MNRAS, 358, 563
Merrett, H. R., et al. 2006, MNRAS, 369, 120
Montalto, M., Seitz, S., Riffeser, A., Hopp, U., Lee, C., & Schönrich, R. 2009, A&A, 507, 283
Nedialkov, P., Berkhuijsen, E. M., Nieten, C., & Haas, M. 2000, in Proc. 232, WE-Heraeus Seminar, ed. E. M. Berkhuijsen, R. Beck, & R. A. M. Walterbos (Aachen: Shaker Verlag), 85
Nieten, C., Neininger, N., Guélin, M., Ungerechts, H., Lucas, R., Berkhuijsen, E. M., Beck, R., & Wielebinski, R. 2006, A&A, 453, 459
Pagani, L., Lequeux, J., Cesarsky, D., Donas, J., Milliard, B., Loinard, L., & Sauvage, M. 1999, A&A, 351, 447
Pettini, M., & Pagel, B. E. J. 2004, MNRAS, 348, L59
Pilyugin, L. S., Ferrini, F., & Shkvarun, R. V. 2003, A&A, 401, 557
Rich, R. M. 1987, AJ, 94, 651
Ruiterkamp, R., Cox, N. L. J., Spaans, M., Kaper, L., Foing, B. H., Salama, F., & Ehrenfreund, P. 2005, A&A, 432, 515
Salama, F., Bakes, E. L. O., Allamandola, L. J., & Tielens, A. G. G. M. 1996, ApJ, 458, 621
Sarre, P. J. 2006, J. Mol. Spectrosc., 238, 1
Sarre, P. J., Miles, J. R., Kerr, T. H., Hibbins, R. E., Fossey, S. J., & Somerville, W. B. 1995, MNRAS, 277, L41
Schlegel, D. J., Finkbeiner, D. P., & Davis, M. 1998, ApJ, 500, 525
Sembach, K. R., Danks, A. C., & Savage, B. D. 1993, A&AS, 100, 107
Snow, T. P. 2002a, ApJ, 567, 407

Snow, T. P. 2002b, in 17th IAP Colloq. on Gaseous Matter in Galaxies and Intergalactic Space, ed. R. Ferlet, M. Lemoine, J. M. Désert, & B. Raban (Paris: Frontier Group), 63
Snow, T. P., Bakes, E. L. O., Buss, R. H., Jr., & Seab, C. G. 1995, A&A, 296, L37
Snow, T. P., & McCall, B. J. 2006, ARA&A, 44, 367
Sollerman, J., Cox, N., Mattila, S., Ehrenfreund, P., Kaper, L., Leibundgut, B., & Lundqvist, P. 2005, A&A, 429, 559
Steidel, C. C., Rich, R. M., & McCarthy, J. K. 1990, AJ, 99, 1476
Thilker, D. A., et al. 2005, ApJ, 619, L67
Thoene, C. C., Michalowski, M. J., Leloudas, G., Cox, N. L. J., Fynbo, J. P. U., Sollerman, J., Hjorth, J., & Vreeswijk, P. M. 2009, ApJ, 698, 1307
Thorburn, J. A., et al. 2003, ApJ, 584, 339
Tielens, A. G. G. M. 2008, ARA&A, 46, 289
Trundle, C., Dufton, P. L., Lennon, D. J., Smartt, S. J., & Urbaneja, M. A. 2002, A&A, 395, 519
van den Bergh, S. 1964, ApJS, 9, 65
van den Bergh, S. 1975, A&A, 41, 53
Vergely, J.-L., Ferrero, R. F., Egret, D., & Koeppen, J. 1998, A&A, 340, 543
Walborn, N. R., & Fitzpatrick, E. L. 1990, PASP, 102, 379
Walterbos, R. A. M., & Braun, R. 1994, ApJ, 431, 156
Wegner, W. 1994, MNRAS, 270, 229
Welty, D. E., Federman, S. R., Gredel, R., Thorburn, J. A., & Lambert, D. L. 2006, ApJS, 165, 138
Xu, C., & Helou, G. 1994, ApJ, 426, 109
York, B. A., Ellison, S. L., Lawton, B., Churchill, C. W., Snow, T. P., Johnson, R. A., & Ryan, S. G. 2006, ApJ, 647, L29